Silicon-based Photonic Devices: Design, Fabrication and Characterization

Ziyang Zhang

Stockholm, 2008

Doctoral Thesis
Department of Microelectronics and Applied Physics
Royal Institute of Technology (KTH)

Akademisk avhandling som med tillstånd av Kungliga Tekniska Högskolan framlägges till offentlig granskning för avläggande av teknologie doktorsexamen i datalogi fredag den 7 mars klockan 10.00 i N1, Electrum 3, Kungliga Tekniska Högskolan, Isafjordsgatan 28, Kista, Stockholm.

Abstract

The field of Information and Communication Technologies is witnessing a development speed unprecedented in history. Moore's law proves that the processor speed and memory size are roughly doubling each 18 months, which is expected to continue in the next decade. If photonics is going to play a substantial role in the ICT market, it will have to follow the same dynamics. There are mainly two groups of components that need to be integrated. The active components, including light sources, electro-optic modulators, and detectors, are mostly fabricated in III-V semiconductors. The passive components, such as waveguides, resonators, couplers and splitters, need no power supply and can be realized in silicon-related semiconductors. The prospects of silicon photonics are particularly promising, the fabrication is mostly compatible with standard CMOS technology and the on-chip optical interconnects are expected to increase the speed of microprocessors to the next generation.

This thesis starts with designs of various silicon-based devices using finite-difference time-domain simulations. Parallel computation is a powerful tool in the modeling of large-scale photonic circuits. High Q cavities and resonant channel drop filters are designed in photonic crystal platform. Different methods to couple light from a single mode fiber to silicon waveguides are studied by coupled-mode theory and verified using parallel simulations. The performance of waveguide grating coupler for vertical radiation is also studied.

The fabrication of silicon-based photonic devices involves material deposition, E-beam or optical lithography for pattern defining, and plasma/wet-chemistry etching for pattern transfer. For nanometer-scaled structures, E-beam lithography is the most critical process. Depending on the structures of the devices, both positive resist (ZEP520A) and negative resist (maN2405) are used. The proximity and stitch issues are addressed by careful dose correction and patches exposure. Some examples are given including photonic crystal surface mode filter, micro-ring resonators and gold grating couplers. In particular, high Q (2.6×10^5), deep notch (40 dB) and resonance-splitting phenomenon are demonstrated for silicon ring resonators.

It is challenging to couple light into photonic integrated circuits directly from a single-mode fiber. The butt-coupled light-injecting method usually causes large insertion loss due to small overlap of the mode profiles and large index mismatch. Practically it is not easy to cleave silicon sample with smooth facet where the waveguide exposes. By adding gold gratings to the waveguides, light can be injected and collected vertically from single-mode fiber. The coupling efficiency is much higher. There is no need to cleave the sample. The access waveguides are much shortened and the stitch problem in E-beam lithography is avoided.

In summary, this thesis introduces parallel simulations for the design of modern large-scale photonic devices, addresses various issues with Si-based fabrication, and analyses the data from the characterization. Several novel devices using silicon nanowire waveguides and 2D photonic crystal structures have been demonstrated for the first time.

Acknowledgements

My three-year PhD study has been a solid journey. At times I have had arguments, confusion and frustration, all of which were outshone by the excitement and fulfillment along the way. I am grateful I have worked with so many brilliant people and that I have learned so much from them, both in science and in life.

First, I wish to thank my supervisor, Dr. Min Qiu, for his guidance through the years in all aspects and department head Prof. Lars Thylén, Gunnar Björk and Sebastian Lourdudoss for their support.

Many thanks to the staff at OPQ for creating such a nice work environment. Special thanks to our secretary Eva Andersson for her kindness, and Prof. Anders Karlsson, Bozena Jaskorzynska, Ari Friberg, Shili Zhang, Dr. Urban Westergren, Eilert Berglind, Richard Schatz, Bo Willen, and Per-Erik Hellström for their teaching and support.

I owe my deep gratitude to the staff working in the Electrum lab. In particular, Dr. Matteo Dainese and Lech Wosinski initially trained me for the processing work in the clean room. They have been helping me through my PhD. Cecilia Aronsson and Silvia Corlevi from Replisaurus, Magnus Lindberg and Reza Fatehnia from Acreo, Anders Liljeborg, David Haviland, Adrian Lovan, Johan Walter, and Ninos Poli from Nano-Physics group, all have helped in various aspects in the lab. Many thanks to Dr. Anand Srinivasan, Marcin Swillo, Ilya Sychugov, PhD student Marek Chacinski, Audrey Berrier, Niklas Elfström and Jonas Tidström for their valuable discussion and support.

Dr. Ulf Andersson was teaching me the basics of parallel computation and has been helping me whenever I have problems in simulations. Many thanks to him along with all the staff at Parallel Computation Center (PDC), KTH, and all the staff in Efield AB for their hard work.

I must also thank my fellow researchers, Dr. Dirk Taillaert, Dr. Dries Van Thourhout, Pro. Peter Bienstman and Roel Baets, all from Ghent University, Belgium, for their help and advice in fiber grating couplers. Pro. Yikai Su, Dr. Tong Ye, graduate students Fangfei Liu, Qiang Li, Xiaohui Li, Qingjiang Chang, all from Shanghai Jiaotong University, China, have been kindly helping us measuring ring resonators and setting up the fiber grating coupler system. Many thanks to Dr. William Whelan-Curin and Pro. Thomas F. Krauss, both from St. Andrews University, Scotland, for helping us fabricate high Q photonic crystal slab cavities.

Finally, I would like to thank my parents. Ordinary as they are, they have shown their son what a good heart is. Once a street brat dreamed about traveling around the world and becoming a doctor. Now it is reality. I hope I have made them proud.

Contents

International Journal Publications

1) <u>Z. Zhang</u> and M. Qiu, "Small-volume waveguide-section high Q microcavities in 2D photonic crystal slabs," Optics Express 12, 3988-3995 (2004)

2) <u>Z. Zhang</u> and M. Qiu, "Influence of structural variations on high-Q microcavities in two-dimensional photonic crystal slabs," Optics Letters 30, 1713-15 (2005)

3) <u>Z. Zhang</u> and M. Qiu, "Compact in-plane channel drop filter design using a single cavity with two degenerate modes in 2D photonic crystal slabs," Optics Express 13, 2596-2604 (2005)

4) <u>Z. Zhang</u> and M. Qiu, "Coupled mode analysis of in-plane channel drop filter with resonant mirrors," Photonics and Nanostructures - Fundamentals and Applications 3, 84-89 (2005)

5) <u>Z. Zhang</u> and M. Qiu, "Coupled-mode analysis of a resonant channel drop filter using waveguides with mirror boundaries," Journal of the Optical Society of America B (Optical Physics) 23, 104-13 (2006)

6) U. Andersson, M. Qiu, and <u>Z. Zhang</u>, "Parallel Power Computation for Photonic Crystal Devices," Methods and Applications of Analysis, vol. 13, 149-156 (2006)

7) <u>Z. Zhang</u>, M. Dainese, L. Wosinski, S. Xiao, M. Swillo, U. Andersson, and M. Qiu, "Optical filter based on two-dimensional photonic crystal surface-mode cavity in amorphous silicon-on-silica structure," Applied Physics Letters 90, 041108 (2007)

8) <u>Z. Zhang</u>, M. Qiu, U. Andersson, and L. Tong, "Subwavelength-diameter Silica Wire for Light In-coupling to Silicon-based Waveguide," Chinese Optics Letters 5, 577 (2007)

9) <u>Z. Zhang</u>, U. Andersson, and M. Qiu, "Subwavelength-diameter Silica Wire and Photonic Crystal Waveguide Slow Light Coupling," Active and Passive Electronic Components, special issue on Metamaterials, Plasmonics, and THz Frequency Photonic Components，Volume 2007, Article ID 78602 (2007)

10) F. Liu, Q. Li, <u>Z. Zhang</u>, M. Qiu and Y. Su, "Optically Tunable Delay Line in Silicon Microring Resonator Based on Thermal Nonlinear Effect," to be published in IEEE. Journal of Selected Topics in Quantum Electronics (2008)

11) <u>Z. Zhang</u>, M. Dainese, M. Chacinski, L. Wosinski, and M. Qiu, "High-quality-factor micro-ring resonator in amorphous-silicon on insulator structure," submitted for journal publication (2008)

12) <u>Z. Zhang</u>, M. Dainese, L. Wosinski, and M. Qiu, "Resonance-splitting and enhanced notch depth in SOI ring resonators with mutual mode coupling," submitted for journal publication (2008)

International Conference/Symposium Participation

1) <u>Z. Zhang</u> and M. Qiu "A Compact Design of In-plane Channel Drop Filter using Degenerate Modes in 2D Photonic Crystal Slabs," The Sixth International Symposium on Photonic and Electromagnetic Crystal Structures (PECS-VI), Crete, Greece, June 19-24, 2005, Contributed Talk

2) M. Dainese, <u>Z. Zhang</u>, M. Swillo, L. Wosinski, M. Qiu, and L. Thylen, "Experimental Demonstration of a Vertically Coupled Photonic Crystal Filter," The 31th European Conference on Optical Communication (ECOC), Glasgow, Scotland, UK, September 25-29, 2005, Contributed Talk

3) <u>Z. Zhang</u>, M. Dainese, L. Wosinski, M. Swillo, U. Andersson, and M. Qiu, "Experimental demonstration of 2D photonic crystal surface cavity in amorphous silicon on silica structure," Optical Fiber Communication Conference (OFC), Anaheim, California, US, March 25-29, 2007, Contributed Talk

4) <u>Z. Zhang</u>, M. Dainese, L. Wosinski, M. Swillo, and M. Qiu, "Two-dimensional photonic crystal surface-mode cavity in amorphous silicon-on-silica structure," The Seventh International Symposium on Photonic and Electromagnetic Crystal Structures (PECS-VII), Monterey, California, US, April 8-11, 2007, Poster Exhibition

5) <u>Z. Zhang</u>, M. Yan, and M. Qiu, "Numerical Studies on Silica Wire Directional Couplers," The Thirteenth European Conference on Integrated Optics (ECIO), Copenhagen, Denmark, April 25-27, 2007, Poster Exhibition

6) <u>Z. Zhang</u>, Q. Li, F. Liu, T. Ye, Y. Su, and M. Qiu, "Wavelength Conversion in a Silicon Mode-split Micro-ring Resonator with 1G Data Rate," submitted to the Conference on Lasers and Electro-Optics (CLEO) 2008

List of symbols and acronyms

7-up	Solution, volume ratio H_2SO_4 (96%) : H_2O_2 (31%) = 4 : 1
α-Si:H	Hydrogenated Amorphous Silicon
AFM	Atomic Force Microscopy
ASE	Amplified Spontaneous Emission
CDF	Channel Drop Filter
CMOS	Complementary metal–oxide–semiconductor
CMP	Chemical-Mechanical Polishing
DUV	Deep-Ultra-Violet (193nm photolithography)
E-beam	Electron Beam Lithography
FDTD	Finite-Different Time-Domain
FIB	Focused Ion Beam (etching)
FSR	Free Spectrum Range
FWHM	Full Width Half Maximum
GEMS	General ElectroMagnetic Solver
GRIN	Gradient Index (fiber lens)
HMDS	Hexamethyldisilazane
ICP	Inductively Coupled Plasma (etching)
ICT	Information and Communication Technology
IPA	Iso-proponal
NA	Numerical Aperture
NMP	N-Methyl-2-Pyrrolindone
PCS	Photonic Crystal Slab
PEC	Perfect Electric Conductor
PECVD	Plasma Enhanced Chemical Vapor Deposition
PhC	Photonic Crystal
PIC	Photonic Integrated Circuits
RMS	Root Mean Square
sccm	Standard Cubic Centimeter per Minute
SEM	Scanning Electron Microscopy
SiO_2-Wr	Silica Wire (waveguide)
Si-Wg	Silicon Wire (waveguide)
SMF	Single Mode Fiber
SOI	Silicon on Insulator (Silica)
STS	Surface Technology Systems[®]
TE	Transverse Electric
TM	Transverse Magnetic
VLSI	Very Large Scale Integration
WDM	Wavelength Division Multiplexing
WGM	Whispery Gallery Mode

Chapter 1.   Introduction

1.1 Background

Take a deep look at the huge success of today's ICT industry and people will be amazed how blessed it is. For one thing, silicon, generously abundant in nature, is a great semiconductor. It can be purified to an unprecedented level. It shows excellent thermal and mechanical stability. It can be easily handled and patterned. The natural oxide of silicon, known as silica, is a perfect insulator, and can be easily grown on silicon. To make things even better, the etching selectivity between silica and silicon is extremely high (10 ~ 100). Another key factor is that the dominating technology, CMOS [1], is pushing the industry to an ever-increasing level of integration. On a Pentium® 4 processor, there are 55,000,000 transistors. The handling wafer size has increased over the years from 100 mm to 300 mm in process and 450 mm is under way, meanwhile single transistor size has been decreasing (gate lengths of 180 nm are in production while 15 nm have been demonstrated) [2].

What happens in the photonic industry is quite a different story. A variety of different materials is used. III-V semiconductors are mostly used for light sources [3] and detectors since bulk silicon is indirect bandgap material and it is difficult to get light emission. Research has proven that silicon nano-particles can work as quantum dots for potential light sources [4]. They have yet to be electrically pumped and improve the performance, mostly increasing light power and reducing noise level at room temperature, to make some practical sense, let alone the complexity involved to prepare the nano-particles. For long-distance waveguiding, germanium doped silica fiber is best suitable. The fiber cables deployed some 10-15 years ago will continue to be used, at least for the next decade. Lithium niobate and other non-linear crystals are good candidates as modulators. Rare-earth elements are used for amplifiers in the WDM networks. No single material or single technology is leading the market. The production technology is diverse and non-standardized. The integration level, in terms of components per unit area, is way behind that of the electronic industry.

Will photonic integration ever achieve similar level as the electronic industry has seen? Probably not. Firstly, it is much more challenging, technically, to integrate the above-mentioned materials on the same chip. There have been efforts to bond III-V active components with SOI waveguides [5-6], however it is still a long way to achieve full functionality, that is, light generation, modulation, transmission, amplification and detection, all in one package. Secondly, from quantum mechanics' point of view, electrons are fermions (matter particles) and they can be confined much more easily than photons (bosons, radiation particles). Considering an electron being accelerated in SEM column by 10kV voltage, the de Broglie wavelength is roughly 12.3 pm, still three orders of magnitude smaller than the 15nm transistor gate-length demonstrated. Electronic devices can keep shrinking in size without running into problems when the wave nature of electrons takes major effect. On the other hand, the use of silica fiber as low-cost yet high-performance data links in long-haul telecommunication networks mostly dictates that the operation wavelength for most photonic devices is clamped in the window 1300

nm - 1600 nm. The mode-field diameter in standard single mode fibers is around 6-8 µm. Most commercial planar photonic devices have minimum feature size on the wavelength level. Though sub-wavelength light confinement is a hot research field, such as plasmonic waveguides, resonators, and etc., they will probably remain in research until, magically, the huge loss issues and coupling issues to single mode fibers or other planar dielectric devices are addressed. Finally, from the design's aspect, it lacks an overall guideline and efficient tools on a larger picture. Traditional methods, such as coupled mode theory, perturbation theory, beam propagation method, transfer matrix method, etc, are good for studying one or a few devices, not on the integrated level. Even so, when the device size goes sub-wavelength and/or the coupling between components become strong and non-linear, the above mentioned methods lose their accuracy. FDTD is a powerful tool as it solves Maxwell equations in a brutal-force way and simulates the real-time light flow in certain structures [7]. The design work using FDTD, however, is still a process of trial-and-error in many cases and it is time-consuming. FDTD also demands tremendous amount of computation power. When putting several devices together and various coupling/resonance issues have to be taken into account, the challenge becomes unimaginable.

Nevertheless, silicon photonics is still a booming research area [8-9]. From optical prospective, silicon is an excellent dielectric medium at 1.55 µm wavelength region. The index is high, ranging from 3.4 – 3.6 depending on the growth process. Silica is also transparent at this wavelength, but with lower index around 1.45 - 1.5 depending on the doping. Silicon and silica can be combined easily for index guiding. The fabrication process is mostly compatible with CMOS technology. Low-loss waveguides and other planar devices have been successfully realized on the SOI platform [10-11]. One big driving force is the need to replace electronic interconnects in today's microprocessors, which has become the bottleneck that limits the operating speed of microelectronic devices. Experts project that optical interconnects will be used to connect computer boards in five years, while the use of optical interconnects within the chip is being investigated and will possibly be realized in 10 – 15 years [12].

Closely related to silicon photonics is another heated research area, photonic crystal devices. Back in year 1987, the term "photonic crystals" (PhCs) was first given to periodic arrangement of dielectric materials that allow inhibition of spontaneous light emission [13] and strong photon localization [14]. Two decades have passed, the realization of three dimensional photonic crystals in the optical region remains challenging and very few devices have been reported based on 3D PhCs. Alternatively, two dimensional photonic crystal slabs (2D PCS's) have been proposed [15-16]. The fabrication techniques can be borrowed from the electronic industry. High Q cavities, waveguides and splitters have all been demonstrated [17-19]. However, the future of PhC-based devices, in my opinion, remains uncertain. Indeed, there are very specific application areas, such as photonic crystal fibers in drug delivery [20], but it is unlikely that photonic crystal should become a dominating platform for future photonic devices. Most successful devices demonstrated require fragile membrane structure, which is difficult to integrate with other parts of PICs. In SOI structure, 2D PCS sharply loses its merits. The Q values of the most "well-known" cavities drop down to a few thousands

and the linear operation region in the waveguide becomes even narrower. If one can re-design the cavities that show higher Q factors, it is possible to add these cavities locally, where necessary, to PICs in SOI structure. After all, the small volume of the cavities is an attractive property for dense integration.

1.2 Thesis objectives

A large part of my thesis is devoted to the design and fabrication of PhC related devices, including high Q cavities and resonant channel drop filters. Other photonic devices, such as waveguides and coupled ring resonators are fabricated on SOI. Characterization method has been changed from traditional butt-coupling method to vertical fiber/grating coupling. In more details the objectives were:

1. To design high Q cavities and compact channel drop filters in PhC by FDTD and parallel computation methods.
2. To apply and develop techniques for the fabrication of photonic devices in SOI platform.
3. To solve the light in-coupling issue from single mode fiber to silicon wire waveguide.
4. To characterize the devices fabricated and analyze the results

The thesis is arranged according to the objectives. Chapter 2 gives an overview of FDTD and parallel computation, followed by design examples. Chapter 3 deals with various aspects of fabrication, the problems involved, the difficulties and the solutions. Chapter 4 compares the two characterization methods and shows the advantages of vertical fiber grating coupler. Chapter 5 provides the main results and summarizes the presented work.

Reference:

1. J. T. Clemens, "Silicon Microelectronics Technology," Bell Labs Technical Journal, Vol. 2, No. 4, pp. 76–102, 1997.
2. International Technology Roadmap for Semiconductors, 2000 Update, Interconnect (http://public.itrs.net).
3. T. L. Koch, "Integrated tunable light sources for telecommunications," IEEE 19th International Semiconductor Laser Conference (IEEE Cat. No.04CH37594), p21 (2004).
4. I. Sychugov, "Synthesis and properties of single luminescent silicon quantum dots," doctoral thesis, ISBN 978-91-7178-533-6, KTH, 2006.
5. H. Park, A. Fang, S. Kodama, and J. Bowers, "Hybrid silicon evanescent laser fabricated with a silicon waveguide and III-V offset quantum wells," Opt. Express 13, 9460-9464 (2005).
6. G. Roelkens, D. Van Thourhout and R. Baets, "Laser emission and photodetection in an InP/InGaAsP layer integrated on and coupled to an SOI waveguide circuit", Opt. Express 14, 8154-8159 (2006).

7. K. S. Yee, "Numerical solution of initial boundary value problems involving Maxwell's equations in isotropic media," IEEE Trans. Antennas and Propagation," 14, 302 (1966).
8. T. L. Koch, "Perspectives on photonic integration," The Fourteenth Annual Wireless and Optical Communications Conference, (IEEE Cat. No. 05EX1026), p17 (2005).
9. T. L. Koch, "Opportunities and challenges in silicon photonics," IEEE LEOS Annual Meeting Conference (IEEE Cat. No. 06CH37736C), p2 (2006).
10. Y. Vlasov and S. McNab, "Losses in single-mode silicon-on-insulator strip waveguides and bends," Opt. Express 12, 1622-1631 (2004).
11. T. Baehr-Jones, M. Hochberg, C.Walker and A. Scherer: High-Q ring resonators in thin silicon-on-insulator, Appl. Phys. Lett. 85, 3346 (2004).
12. L. Pavesi, "Will silicon be the photonic material of the third millennium?" J. Phys.: Condens. Matter 15, 1169-1196 (2003).
13. E. Yablonovitch, "Inhibited Spontaneous Emission in Solid-State Physics and Electronics," Phys. Rev. Lett. 58, 2059 (1987).
14. S. John, "Strong localization of photons in certain disordered dielectric superlattices," Phys. Rev. Lett. 58, 2486 (1987).
15. T. F. Krauss, R. M. De La Rue, and S. Brand, "Two-dimensional photonic-bandgap structures operating at near-infrared wavelengths", Nature 383, 699 (1996).
16. S. G. Johnson, S. Fan, P. R. Villeneuve, J.D. Joannopoulos, and L.A. Kolodziejski, "Guided modes in photonic crystal slabs," Phys. Rev. B, 60, 5751 (1999).
17. B. S. Song, S. Noda, T. Asano, and Y. Akahane, "Ultra-high-Q photonic double-heterostructure nanocavity," Nature Materials 4, 207-210 (2005).
18. S. J. McNab, N. Moll, and Yu. A. Vlasov, "Ultra-low loss photonic integrated circuit with membrane-type photonic crystal waveguides," Opt. Express 11, 2927–2939 (2003).
19. S. Shi, A. Sharkawy, C. Chen, D. M. Pustai, and D. W. Prather, "Dispersion-based beam splitter in photonic crystals," Opt. Lett. 29, 617-619 (2004).
20. A. Dupuis, N. Guo, Y. Gao, N. Godbout, S. Lacroix, C. Dubois, and M. Skorobogatiy, "Prospective for biodegradable microstructured optical fibers," Opt. Lett. 32, 109-111 (2007).

Chapter 2.   Simulation

2.1 FDTD background

Finite-Difference Time-Domain method is a powerful tool in solving electromagnetic problems. This method was proposed by Yee in 1966 [1] and further developed by Taflove in the 1970s [2]. It has been widely used to study electromagnetic wave propagation in different structures for antenna design, optical device simulations, and etc.

In linear isotropic source-free material, the Maxwell equations can be written as

$$\frac{\partial \vec{H}}{\partial t} = -\frac{1}{\mu(\vec{r})} \nabla \times \vec{E} \qquad (1)$$

$$\frac{\partial \vec{E}}{\partial t} = \frac{1}{\varepsilon(\vec{r})} \nabla \times \vec{H} - \frac{\sigma(\vec{r})}{\varepsilon(\vec{r})} \vec{E} \qquad (2)$$

Yee suggested a convenient way to discretize Maxwell equations both in time and in space. Fig. 2-1 shows the arrangement of the six field components in a unit FDTD cell, known as the Yee cell. The time stepping for the E and H field components is also interleaved.
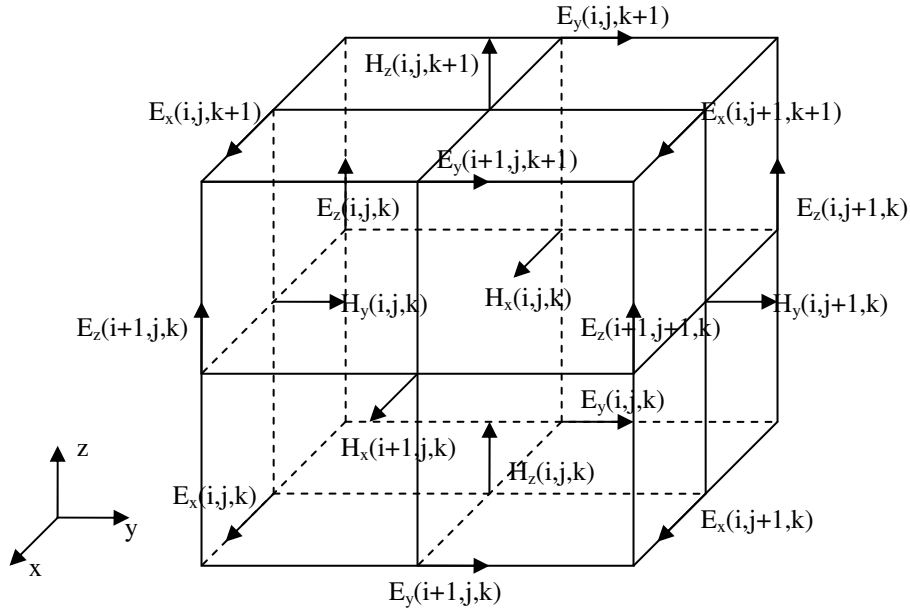

Fig. 2-1. A unit cell of the 3D FDTD mesh using Yee's algorithm.

The discretized Maxwell equations can be written into

$$H_x\Big|_{i,j,k}^{n+1/2} = H_x\Big|_{i,j,k}^{n-1/2} - \frac{\Delta t}{\mu_{i,j,k}} \left(\frac{E_z\Big|_{i,j+1,k}^{n} - E_z\Big|_{i,j,k}^{n}}{\Delta y} - \frac{E_y\Big|_{i,j,k+1}^{n} - E_y\Big|_{i,j,k}^{n}}{\Delta z} \right) \qquad (3)$$

$$H_y\Big|_{i,j,k}^{n+1/2} = H_y\Big|_{i,j,k}^{n-1/2} - \frac{\Delta t}{\mu_{i,j,k}}\left(\frac{E_x\Big|_{i,j,k+1}^{n} - E_x\Big|_{i,j,k}^{n}}{\Delta z} - \frac{E_z\Big|_{i+1,j,k}^{n} - E_z\Big|_{i,j,k}^{n}}{\Delta x}\right) \tag{4}$$

$$H_z\Big|_{i,j,k}^{n+1/2} = H_z\Big|_{i,j,k}^{n-1/2} - \frac{\Delta t}{\mu_{i,j,k}}\left(\frac{E_y\Big|_{i+1,j,k}^{n} - E_y\Big|_{i,j,k}^{n}}{\Delta x} - \frac{E_x\Big|_{i,j+1,k}^{n} - E_y\Big|_{i,j,k}^{n}}{\Delta y}\right) \tag{5}$$

$$E_x\Big|_{i,j,k}^{n+1} = \frac{\varepsilon_{i,j,k} - \sigma_{i,j,k}\Delta t/2}{\varepsilon_{i,j,k} + \sigma_{i,j,k}\Delta t/2}E_x\Big|_{i,j,k}^{n} +$$

$$\frac{\Delta t}{\varepsilon_{i,j,k} + \sigma_{i,j,k}\Delta t/2}\left(\frac{H_z\Big|_{i,j,k}^{n+1/2} - H_z\Big|_{i,j-1,k}^{n+1/2}}{\Delta y} - \frac{H_y\Big|_{i,j,k}^{n+1/2} - H_y\Big|_{i,j,k-1}^{n+1/2}}{\Delta z}\right) \tag{6}$$

$$E_y\Big|_{i,j,k}^{n+1} = \frac{\varepsilon_{i,j,k} - \sigma_{i,j,k}\Delta t/2}{\varepsilon_{i,j,k} + \sigma_{i,j,k}\Delta t/2}E_y\Big|_{i,j,k}^{n} +$$

$$\frac{\Delta t}{\varepsilon_{i,j,k} + \sigma_{i,j,k}\Delta t/2}\left(\frac{H_x\Big|_{i,j,k}^{n+1/2} - H_x\Big|_{i,j,k-1}^{n+1/2}}{\Delta z} - \frac{H_z\Big|_{i,j,k}^{n+1/2} - H_z\Big|_{i-1,j,k}^{n+1/2}}{\Delta x}\right) \tag{7}$$

$$E_z\Big|_{i,j,k}^{n+1} = \frac{\varepsilon_{i,j,k} - \sigma_{i,j,k}\Delta t/2}{\varepsilon_{i,j,k} + \sigma_{i,j,k}\Delta t/2}E_z\Big|_{i,j,k}^{n} +$$

$$\frac{\Delta t}{\varepsilon_{i,j,k} + \sigma_{i,j,k}\Delta t/2}\left(\frac{H_y\Big|_{i,j,k}^{n+1/2} - H_y\Big|_{i-1,j,k}^{n+1/2}}{\Delta x} - \frac{H_x\Big|_{i,j,k}^{n+1/2} - H_x\Big|_{i,j-1,k}^{n+1/2}}{\Delta y}\right) \tag{8}$$

In the equations above, the superscript *n* indicates the number step and the subscript, *i, j, k*, indicate the location of the field in the computational domain. The time step *Δt* is related to the spatial increments *Δx* , *Δy* and *Δz*   by the stability condition [3], i.e.,

$$\Delta t \leq \frac{1}{c_0\sqrt{\Delta x^{-2} + \Delta y^{-2} + \Delta z^{-2}}}, \tag{9}$$

where c_0 is the light speed in vacuum. We can define a coefficient as the relation between the actual time step and the maximum time step allowed. This coefficient is commonly known as the Courant-Friedrichs-Lewy (CFL) number. Some common choices of CFL numbers are 0.866, 0.9 and 0.95.

FDTD updates the field components using the values from the previous time step and one must specify an initial field distribution to trigger the updating. Commonly used source excitations include plane waves, point Gaussian pulses and waveguide eigen-mode excitations.

Special care must be taken at the boundary of the finite computational domain. The boundary can be reflecting, such as perfect electric conductor (PEC) and perfect magnetic conductor (PMC), or absorbing. Commonly used absorbing boundary conditions include first order Mur and perfectly matched layer (PML).

Detailed explanation of FDTD and related issues can be found at Ref.[4-5] and the cited work within.

2.2 Parallel Computation

Back in history, software was written for serial computation, i.e., the programs were run on a single computer having a single Central Processing Unit (CPU). As the demand for large-scale complex simulations grew higher, serial computation proved to be insufficient. Though the CPU speed has increased tremendously over the years, it is still not fast enough, by serial computation alone, to simulate problems such as weather and oceanic patterns, large airport traffic control, atomic level reactions, to name a few.

Parallel computation was proposed in the 1960s. Simply put, parallel computation is the simultaneous use of multiple computer resources, including CPUs and memories, to solve a specific problem. The problem should be easily broken into discrete parts that can be solved concurrently on different computers. Communication is often needed between these computers and the data are collected to form a final solution.

For the design of photonic devices, serial simulations are still being used today, but mainly limited to small-scale problems, such as the study of individual micro-cavities and waveguides. Parallel computation is highly needed. Since photonic devices for telecommunication work mostly around 1550 nm wavelength region and for accurate simulations the cell size is recommended to be smaller than one-tenth of the wavelength [6], the computation domain (in terms of the number of cells) can be extremely large when various photonic components are combined for the design of large scale photonic integrated circuits. In most cases memory requirements alone will exclude the use of serial simulations. Moreover, the simulation time depends on how fast light propagates through the waveguides and how strong the couplings are in the resonators. For slow-light in the waveguide (for delay lines, light storage, etc) and high Q resonators, the simulation time can be extremely long before the wave stabilizes. Parallel computation can shorten the simulation time almost linearly, in the best scenario, and therefore improve the design efficiency.

Thankfully, the kernel Yee algorithm in FDTD can be easily parallelized. The computation domain is divided into sub-blocks. Each computer node can take care of one block and communicate with its neighbors for data-sharing within each time step.

In this thesis, two sets of simulation tools are used. The serial version, including both 2D and 3D FDTD programs, has been developed by Dr. Min Qiu [7]. I have used these codes to design high Q micro-cavities and resonant channel drop filters in photonic crystal slabs. The parallel version is called the General ElectroMagnetic Solver (GEMS). The codes were developed by the Parallel and Scientific Computing Institute (PSCI) in Sweden, are written in Fortran 90, parallelized using the Message Passing Interface (MPI), and run on a variety of parallel computers [8]. Now the spin-off company Efield AB [9] is further developing and commercializing the GEMS codes. The GEMS time-domain code MBfrida is a multi-block solver based on a hybrid between the FDTD

method on structured grids and the finite-element time-domain (FETD) method on unstructured grids. Due to the compact structure in my simulations, the hybrid grid method is not used. I have used MBfrida to simulate various large-scale waveguide coupling structures. The simulations were done on the Lucidor cluster [10], KTH. The cluster is memory-distributed system. It consists of 74 HP rx2600 servers and 16HP zx6000 workstations, each with two 900MHz Itanium 2 (McKinley) processors and 6 Gigabyte main memory. Since FDTD is a memory bandwidth limited algorithm, there is no point in using more than one processor per node [11]. The network bandwidth (bi-directional) is 489Mbyte/s and the latency is 6.3 ms.

2.3 Various resonant channel drop filters in photonic crystals

2.3.1 Single cavity with two degenerate modes

There have been different designs of channel drop filters in Two-dimensional photonic crystal slabs (2D PCS). The surface-emitting type [12-15] consists of a waveguide and a cavity system. Input signal from the waveguide tunnels into the cavity and is emitted in the vertical direction. Though in principle all light can be dropped in the vertical direction by using a cavity system with two degenerate modes [15], this design brings up a real challenge when collecting light vertically. The in-plane design involves two waveguides (bus and drop) and a cavity system. Theoretical analysis of the in-plane channel drop filter has matured over the years [16-18] and in principle 100% transfer between two waveguides can be realized if the cavity system provides at least a pair of degenerate modes of opposite symmetry with infinitely high vertical Q factor. Yet very few in-plane designs in 2D PCS's have been reported [19-20]. The bottleneck lies in the cavity system, which largely limits the drop efficiency (loss) and line-width of the filter.

In 2D PCS light is confined vertically by index-guiding. Cavity modes are always leaky in the vertical direction. For a symmetric in-plane channel drop filter system where the degenerate modes have equal frequency and equal decay rates into both waveguides, the power transmission $|\mathbf{T}|^2$ and power dropped $|\mathbf{D}|^2$ at resonance can be expressed by [17],

$$|T|^2 = \left(\frac{1}{1+2\tau_o/\tau_e}\right)^2 = \left(\frac{1}{1+2Q_o/Q_e}\right)^2 \approx \left(\frac{1}{1+Q_\perp/Q_\parallel}\right)^2 \qquad (11)$$

$$|D|^2 = \left(\frac{2}{2+\tau_e/\tau_o}\right)^2 = \left(\frac{2}{2+Q_e/Q_o}\right)^2 \approx \left(\frac{1}{1+Q_\parallel/Q_\perp}\right)^2 \qquad (12)$$

where $1/\tau_o$ is the decay rate due to loss and $1/\tau_e$ is the decay rate into either waveguide. The decay rate is related to Q factor by $Q_o = \omega_0\tau_o/2$ and $Q_e = \omega_0\tau_e/2$. If the resonant frequency ω_0 of the cavity modes lies within the lossless region of the waveguide, the total loss of the system is mainly from the vertical radiation of the cavity, i.e., $Q_o \approx Q_\perp$, where $Q_\perp$ is the vertical Q factor of the cavity. The in-plane Q factor ($Q_{//}$) of the cavity is related to Q_e by $Q_{//} = Q_e/2$ if we assume the cavity modes decay into both waveguides equally and ignore the in-plane loss due to the limited number of lattice surrounding the system. From equation (1) and (2), we can see the direct relation between the drop efficiency and the ratio $Q_\perp/Q_{//}$. For example, in order to have $|\mathbf{D}|^2 > 80\%$, $Q_\perp$ should at least be 10 times larger than $Q_{//}$. The choice of high Q cavity is critical.

In the first example, a compact design of in-plane channel drop filter (CDF) is demonstrated using a single cavity that supports two high Q modes. The serial version of the 3D FDTD code is used for main simulations. A combination of FDTD techniques and Padé approximation with Baker's algorithm [21-22] is used for the cavity mode Q factor calculations.

The structure of the cavity is shown in Fig. 2-2 (a). This cavity is constructed by a central large air hole with radius R_0, surrounded by 4 periods of air holes with decreasing radii, along the outward direction denoted by R_1, R_2, R_3, and R_4 respectively. The radius of the air holes on the same hexagon stays the same and R_1 to R_4 follows a parabolic pattern as shown in Eq. (13). The radius of air holes on the outmost hexagon R_4 is the same as the regular air hole radius $R = 0.30a$, where a is the lattice constant and set to *420nm* in our case. The slab thickness t is *0.6a* and the refractive index n of the slab is *3.4*, corresponding to silicon at *1.55μm*. If R_0 and R_1 are given, the cavity structure is determined.

$$R_m = R_1 - (m-1)^2 (R_1 - R_4)/9; m = 1,2,3,4. \qquad (13)$$
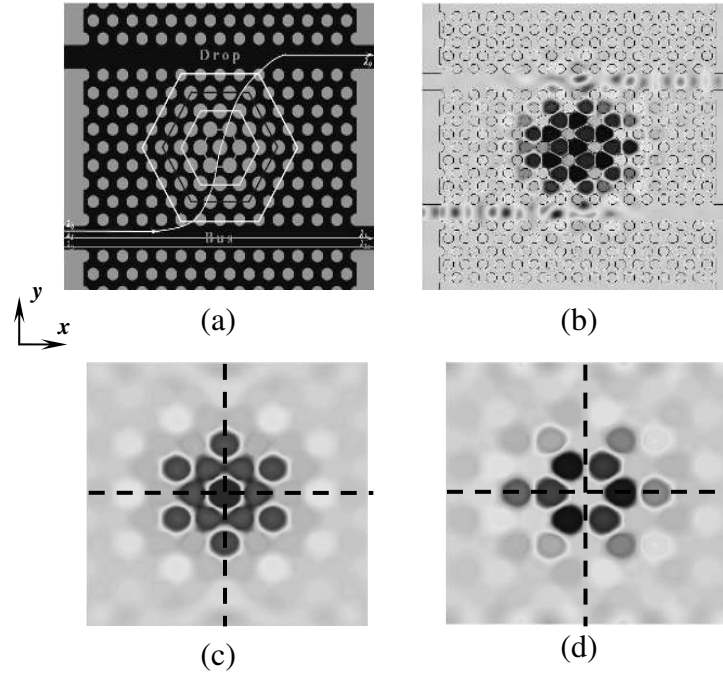

(a) (b)

(c) (d)

Fig. 2-2 (a) Top view of the system. Selected channel is transferred along the forward direction of the drop waveguide. The cavity involves a central large air hole surrounded by 4 hexagons of lattice. The radii of air holes on the hexagons are tuned into a graded pattern following Eq. (13). (b) Snap shot of the wave propagation at resonance. (c) H_z field distribution of the even mode at central slab plane. (d) H_z field distribution of the odd mode at central slab plane. The mirror planes are shown as the dashed lines.

This cavity consists of two-levels of vertical light confinement [23]. The first level of confinement has a centrally enlarged air hole (R_0) followed by a relatively large decrease in hole radius (R_1) for the nearest neighbor holes. The radii are then parabolically decreased in moving radially outwards down to $R_4 = R$ at the edge of the cavity, forming

the second level of confinement. Though increasing the number of hexagons surrounding the central large hole can enhance the vertical light confinement, it also reduces waveguide-cavity coupling. The hexagonal symmetry of the cavity itself makes it possible to support two modes of opposite symmetries (though only the mode with H_z field even in both in-plane directions was reported in Ref. [23]). As shown in Fig. 2-2 (c) and (d), the first mode has H_z field even in both x and y directions and the second mode has H_z field even along y direction but odd along x direction. Their symmetry properties decide a forward drop when the two modes are degenerate [17]. When R_1 is $0.372a$, the two modes have closest central wavelengths as well as Q factors, with $\lambda_1 = 1554.51$nm, $\lambda_2 = 1554.52$nm, $Q_1 = 3,060$ and $Q_2 = 3,020$. Further computation separates $Q_\perp$ and $Q_{//}$ from Q total by $Q^{-1} = Q_\perp^{-1} + Q_{//}^{-1}$. For the even mode, $Q_{\perp 1} = 40,500$ and $Q_{//1} = 3,100$. For the odd mode, $Q_{\perp 2} = 35,000$ and $Q_{//2} = 3,050$. The central wavelength difference is smaller than $0.01nm$ and is negligible compared to the line width.

The simulation result for the power transmission is shown in Fig. 2-3. At resonance, *78%* of light power is transferred along the forward direction of the drop waveguide, *1.75%* is transferred along the backward direction of the drop waveguide, and *1.6%* is still left in the bus waveguide. The Q factor measured as full width half maximum (FWHM) of the transmission spectrum is around *3,000*, relevant to the previous $Q_{//}$ calculations. Detailed tuning process and other issues related to this CDF design are included in Paper III.
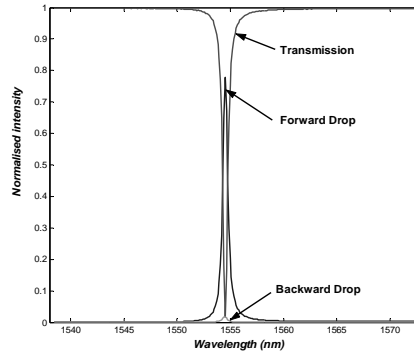

Fig. 2-3 Power transmission spectra for the CDF design in Fig. 2-2.

2.3.2 Resonant mirror systems

The design of cavity with two degenerate high Q modes is difficult. Alternatively, we can add mirror boundaries to the waveguides and only require the cavity to support one high Q mode. Detailed analysis using coupled mode theory can be found in Paper IV and V. The resonant frequency and the system Q factor are dependant on the phase term introduced by reflection at the mirror and wave propagation between the two ports. The relation between the system quality factor and the resonant frequency is a closed curve. The two-mirror system can work as a channel drop filter if two identical mirrors are placed symmetrically to the cavity center. With the absence of mirror loss and negligible

intrinsic system loss, 100% channel transfer can be achieved. The system is realized in 2D photonic crystals by 2D serial FDTD simulations (F2P). The results are shown in Fig. 2-4.
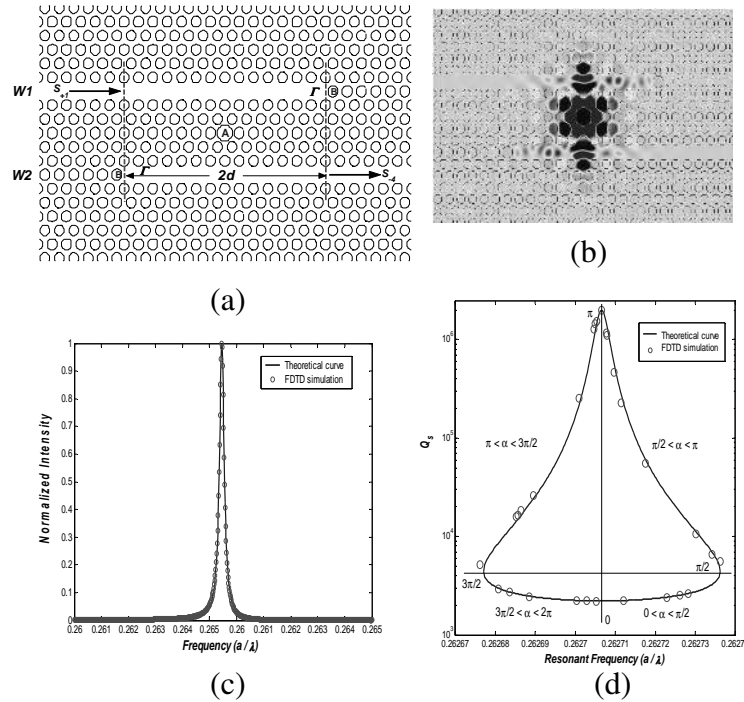

(a)

(b)

(c)

(d)

Fig. 2-4 CDF in 2D PhC using a single mode cavity and two waveguides with mirror boundaries. The mirrors are applied by terminating the waveguide with crystal lattice. (a) schematic of the filter. (b) H_z field distribution when the phase delay is $2k\pi + \pi$. A point Gaussian pulse is placed inside the cavity as light source. (c) Transmission spectrum from port 1 to port 4. (d) The system Q factor and the resonant frequencies are related in a closed curve.

In the previous analysis we have assumed the mirror to be frequency independent. Though 100% channel transfer can be realized theoretically, it reflects all the other channels back to port 1 and other devices will have to be used to separate the reflected channels from the input ones. If we can terminate the waveguides with wavelength selective mirrors so that only the selected channel is reflected, the other channels can just pass through. While there exist various designs of wavelength selective mirrors, one simple way is to use the same single mode cavity as a resonant mirror. Fig. 2-5 (a) shows the system with one resonant mirror replaced. Fig. 2-5 (c) shows the three-cavity system, in which the central cavity decays into both waveguides while the side cavities reflect the resonant channel back into the system. The transmission spectra are shown in Fig. 2-5 (b) and (d), respectively. The side lobes of the backward drop in the three-cavity system can be suppressed by changing the decay rate of cavity A_1.

In photonic crystals the tuning of the cavity is usually completed by changing some structural parameters such as air hole radius and position. However, this tuning often leads to the changes in the cavity/waveguide and cavity/cavity coupling. The mixed tuning process complicates the CDF design where cavities are coupled. The advantage of

the resonant mirror CDFs is that the direct coupling between the cavities is not required. The cavities can be tuned independently and locally so they have the same resonant frequency and desired decay rates into the waveguides.
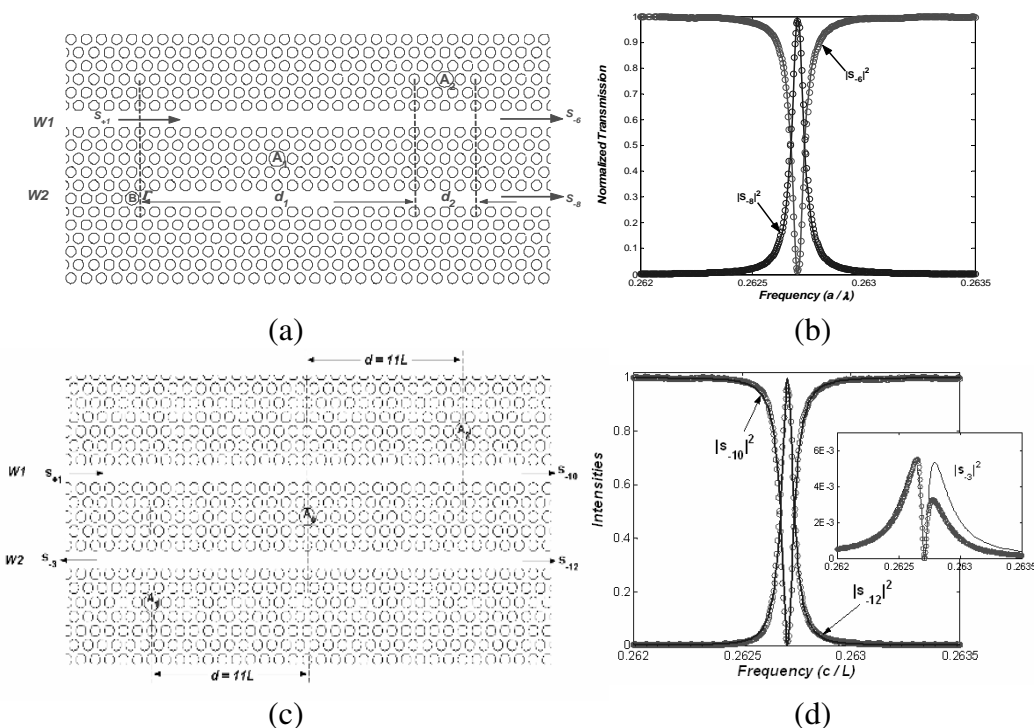

Fig. 2-5 (a) Port 4 is terminated by a resonant mirror A_2, which is also a single mode cavity. Dielectric constant of the material inside hole A_2 is tuned so that the cavity mode has the same resonant frequency and decay rate into W1 as A_1. (b) Transmission spectra of the resonant mirror CDF. (c) Three-cavity systems, with A_1 and A_2 as resonant mirrors. (d) Transmission spectra of the three-cavity CDF. In (b) and (d), the solid curves are plotted using coupled mode analysis and the circles are data obtained from FDTD simulations.

2.4 Light in-coupling to silicon waveguides

Silicon wire waveguides (Si-Wg), with typical cross-section around 250 nm by 450 nm, have been widely used for modern PICs. However, it is challenging to couple light directly from a conventional single-mode fiber (SMF) with core diameter ~ 6.5 μm. The butt-coupled light-injecting method usually causes large insertion loss due to the small overlap of the mode profile and index mismatch. There are a few solutions. One can taper the silicon waveguide to a few microns, similar to the SMF core diameter. The taper length has to be increased to a few hundred microns to reduce the coupling into the radiation modes and still the back reflection in the taper is inevitable. Another solution is to use tapered fibers (SiO$_2$-Wr) as discussed in Paper VIII. When the fiber diameter decreases to around 1 μm, the coupling efficiency can be improved greatly. The fiber then becomes air-clad and the practical problem is how to hold the fiber in place without disturbing the light propagation. Polymer or silica inverse taper (mode size converter) was also proposed [24-26]. The insertion loss is only around a few dB. This requires

precise fabrication control to bring down the tip of the silicon wire to below 100 nm. The structure also becomes bulky in the vertical dimension. Vertical fiber/grating coupler is another popular solution. It uses in-plane gratings to couple light out-of-plane from fiber to silicon wire [27-30]. The coupling efficiency ranges from 30% - 70%. It is similar to the probing testing technique used in electronics and seems ideal for testing PICs since the fiber tips can be brought into close proximity and the access waveguides can be short enough to fit into one E-beam write field.

2.4.1 Single mode fiber and silicon waveguide butt-coupling

It is interesting to see, in 3D simulations, how inefficient the direct butt-coupling between SMF and Si-Wg really is, as previous studies were done mostly in 2D analysis. Thanks to the parallel code (MBfrida), we are able to compute fine-grid, large-scale photonic circuits in a relatively short time. The structure schematic is shown in Fig. 2-6(a). The diameter of the fiber core is 6.5 μm and the refractive index is 1.4618 at 1.55 μm region. The cladding index is 1.4529. The cladding diameter is reduced to 20 μm to facilitate computation, which is justified considering the mode field diameter is around 7.5 μm. The silicon waveguide is 450 nm wide along the x direction and 250 nm thick along the z direction. The refractive index of silicon is 3.6. The fiber axis and the Si-Wg center axis are aligned along the y direction. Light travels in silicon waveguide 15μm before we measure the power flow through a small window. The window size is only 1μm along x and 500 nm along z. In this way, we can incorporate the majority of guided mode power and exclude the scattered light from the SMF/Si-Wg interface.
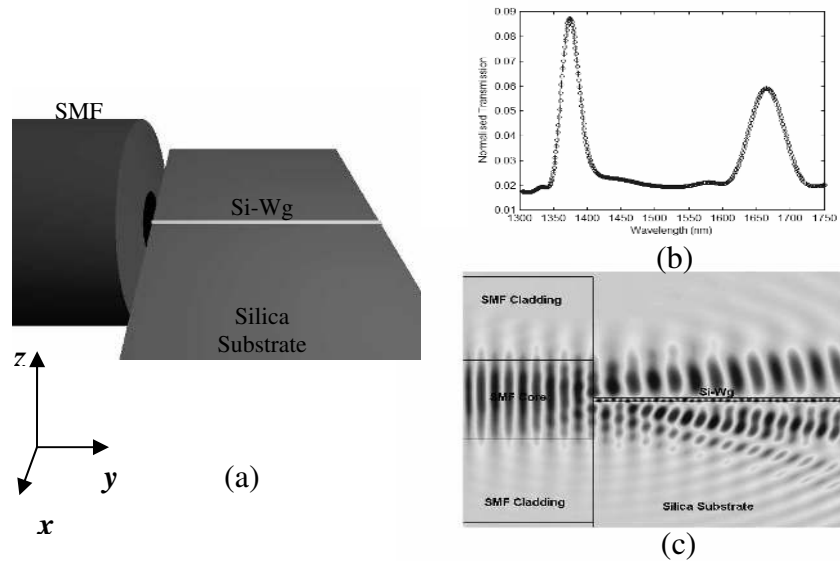

Fig. 2-6 (a) Schematic of SMF and Si-Wg butt-coupler. (b) Power transmission. (c) E_x field distribution at central YZ plane for 1550 nm wavelength.

The power transmission result is shown in Fig. 2-6(b). There are two peaks at 1375 nm and 1665 nm, probably due to the maximum mode matching for TM-like and TE-like

guided Si-Wg modes, respectively. At 1.55-µm wavelength region, only 2% of coupling efficiency is observed. Fig. 1(c) clearly demonstrates that most light (E_x field) is either scattered above in the air region or leaking away into the substrate.

2.4.2 Tapered fiber and silicon waveguide butt-coupling

With reduced fiber diameter, the SiO_2-Wr mode and Si-Wg mode share a larger overlap and the coupling efficiency should increase. The schematic is shown in Fig. 2-7(a). H_s is the spacing along y direction between the surfaces of SiO_2-Wr and Si-Wg. O_s and V_s are the axial misalignments. The SiO_2-Wr radius is chosen to be 1µm and the refractive index is lumped into 1.5. H_s, O_s and V_s are all set to zero. The power transmission result is shown in Fig. 2-7(b) and much reduced scattering is observed in Fig. 2-7(c). The lateral E_x field across Si-Wg is shown in Fig. 2-7(d) and it matches the guided fundamental TE-like mode. More than 40% of light is transferred from SiO_2-Wr to Si-Wg for wavelength range from 1300 to 1750 nm. Similar transmission result is obtained when injecting light from Si-Wg and out-coupling from SiO_2-Wr. Detailed analysis of axial misalignments and fiber radii issues are included in Paper VIII.

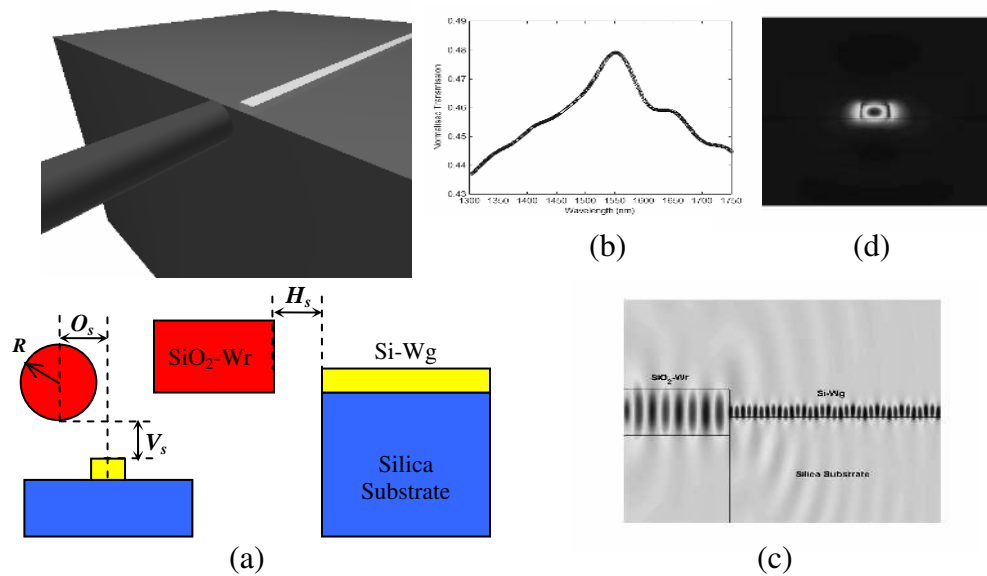Fig. 2-7. (a) Schematic of SiO_2-Wr and Si-Wg butt-coupler. (b) Power transmission. (c) E_x field distribution at central YZ plane for 1550-nm wavelength. (d) Lateral (XZ) distribution of E_x field in Si-Wg.

2.4.3 Tapered fiber and silicon waveguide directional coupling

To explore SiO_2-Wr and Si-Wg coupling even further, their evanescent directional coupling is studied. The structure is shown in Fig. 2-8 (a). To prevent light leakage into the silica substrate, the beginning section of the silicon wire is suspended in air. Since the propagation constants in these two waveguides are significantly different, light cannot be completely transferred from one waveguide to the other. On the other hand, if the

coupling is strong, high power transfer can still take place. Coupled mode analysis based on weak-coupling assumptions is not justified and the system has to be solved numerically. In our simulations, the two waveguides are brought into contact to improve coupling. The interacting distance L is approximately the same as the overlapping distance of the two waveguides. We vary L in search for the maximum power transmission. The results are shown in Fig. 2-8 (b). As L goes from 1 to 6 μm, the power transferred from SiO_2-Wr to Si-Wg increases. At overlapping distance 6 μm, 81% peak transmission occurs at 1575 nm with 3-dB bandwidth around 100 nm. When L further increases, the peak transfer power starts to drop.
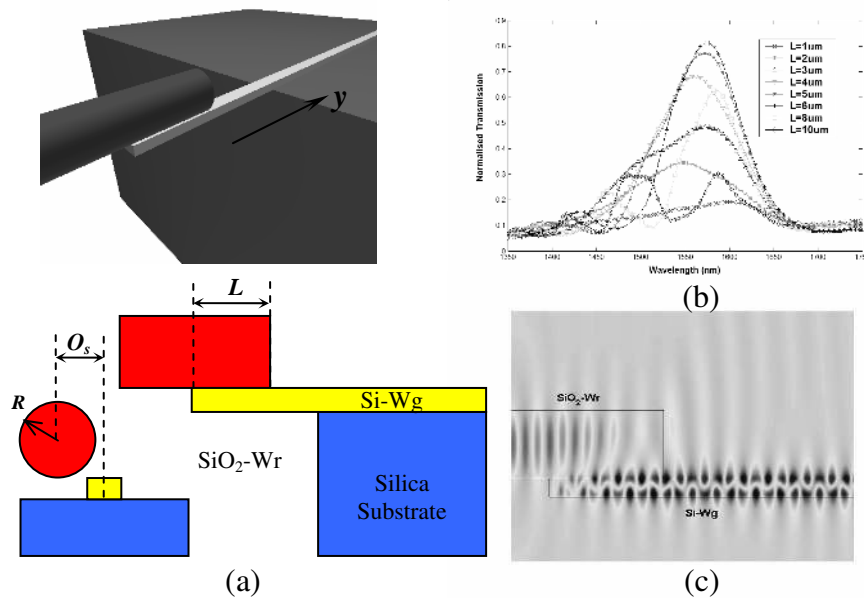

Fig. 2-8. (a) Schematic of SiO_2-Wr and Si-Wg directional coupler. (b) Power transmission at different overlapping distance L. (c) E_x field distribution at central YZ plane for 1575nm wavelength.

However, unlike in the butt-coupling case, from Fig. 2-8 (c) we see that the waveguide mode in Si-Wg generated from directional coupling is not simply TE-like. In fact air-suspended Si-Wg with cross-section 450 nm by 250 nm supports 4 eigen-modes while the same wire on silica substrate only supports two, i.e., the fundamental TE and TM modes. Further studies reveal that this strong interaction from SiO_2-Wr excites mostly higher-order mode. The junction loss between air-suspended and silica-substrated Si-Wg is rather high and only 1% of light is measured transmitting from SiO_2-Wr to silica-substrated Si-Wg. This strong directional coupling is only favorable in generating higher-order modes in air-suspended Si-Wg and is inefficient to couple light to silica-substrated Si-Wg.

2.4.4 Inverse taper mode converter

In the inverse taper mode converter, Si-Wg is partly covered by silica or polymer upper cladding with index close to SMF. The cross-section of the cladding is also compatible

with SMF mode field diameter for better mode overlapping. Light transmits from SMF to silica/polymer cladding waveguide with high efficiency. The Si-Wg is tapered down to a nanometer-sized tip, the mode field profile becomes delocalized from the waveguide core. This delocalization increases the mode overlap with the cladding mode. Light then transmits gradually from the cladding into the silicon core.

The schematic is shown in Fig. 2-9 (a). We only simulate the part, where light transmits from the silica/polymer cladding into Si-Wg. The silica substrate is 3 μm thick, the cross-section of the silica/polymer cladding is 3 μm by 3 μm. Si-Wg cross-section is 450 nm by 250 nm. The taper length is 10 μm. The reference power plane is placed in the silica/polymer cladding 8 μm in front of the starting point of the taper. The transmission power plane is placed in the Si-Wg 8 μm behind the end of silica cladding. Various taper tip sizes are simulated and the results are shown in Fig. 2-9 (b). When the tip size is below 100 nm, more than 80% of light can be transmitted from silica/polymer cladding into Si-Wg for a broad wavelength region.
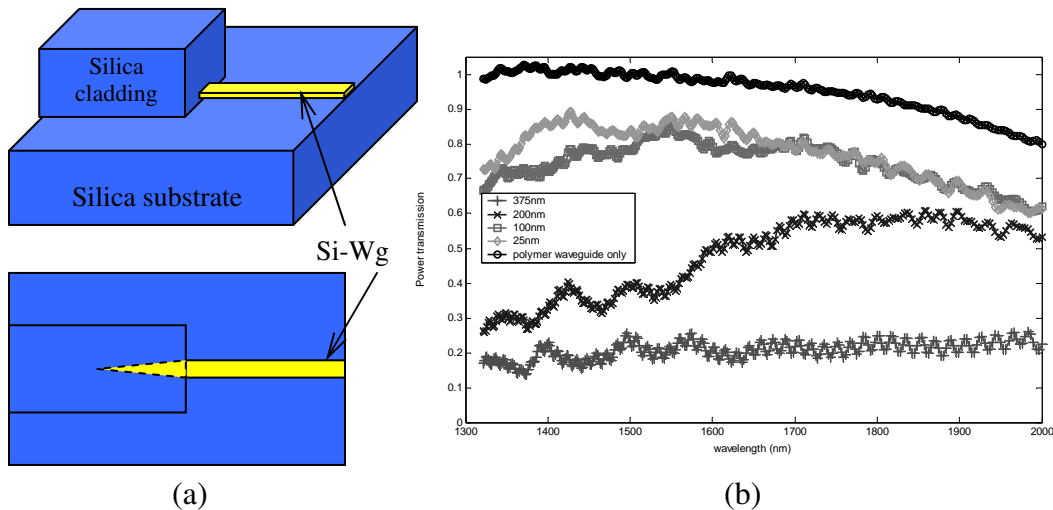

Fig. 2-9. (a) Schematic of the inverse taper mode converter. (b) Power transmission with respect to different silicon taper tip sizes.

2.4.5 Vertical grating couplers

Vertical fiber grating couplers have been studied extensively in Ghent University. For the un-modulated silicon gratings, more than 30% coupling efficiency has been demonstrated experimentally. The coupling efficiency can be further increased by tuning the grating period, coating the substrate with a reflecting layer such as gold, and adding silica/polymer upper cladding. Their simulations are mostly based on 2D eigenmode expansion tools [31]. In the first step, reflection and transmission of the entire structure is calculated. Secondly, the coupling efficiency is calculated from the integral of the radiated field and the Gaussian fiber waveguide mode.

Using MBfrida, I have simulated the 3D structure and calculated the mode distribution and the vertical power transmission for both silicon grating and metal grating couplers.

The structure is shown in Fig. 2-10 (a). Top silicon layer is 250 nm and the silica substrate is 3 μm thick. Since the reflection at the interface between substrate silica and bottom silicon wafer affects the amount of light radiated upwards, 0.5 μm silicon bottom layer is added in the simulations. The waveguide is 5 μm wide and 22.5 μm long. For silicon gratings, the air trench (etching depth) is 75 nm deep. For metal gratings, the metal stripe is 25 nm thick, i.e., one FDTD cell. The metal is approximated by PEC. This approximation is justified because gold and silver work as nearly perfectly reflecting mirrors at 1550 nm wavelength region. The periodic presence of metal stripes only introduces perturbation to the silicon waveguide and facilitates the coupling into radiation modes in air. The incident power plane, as reference, is put in the waveguide 10 μm in front of the start of gratings. The transmission plane to measure the vertical radiation is placed 2.5 μm above the waveguide.
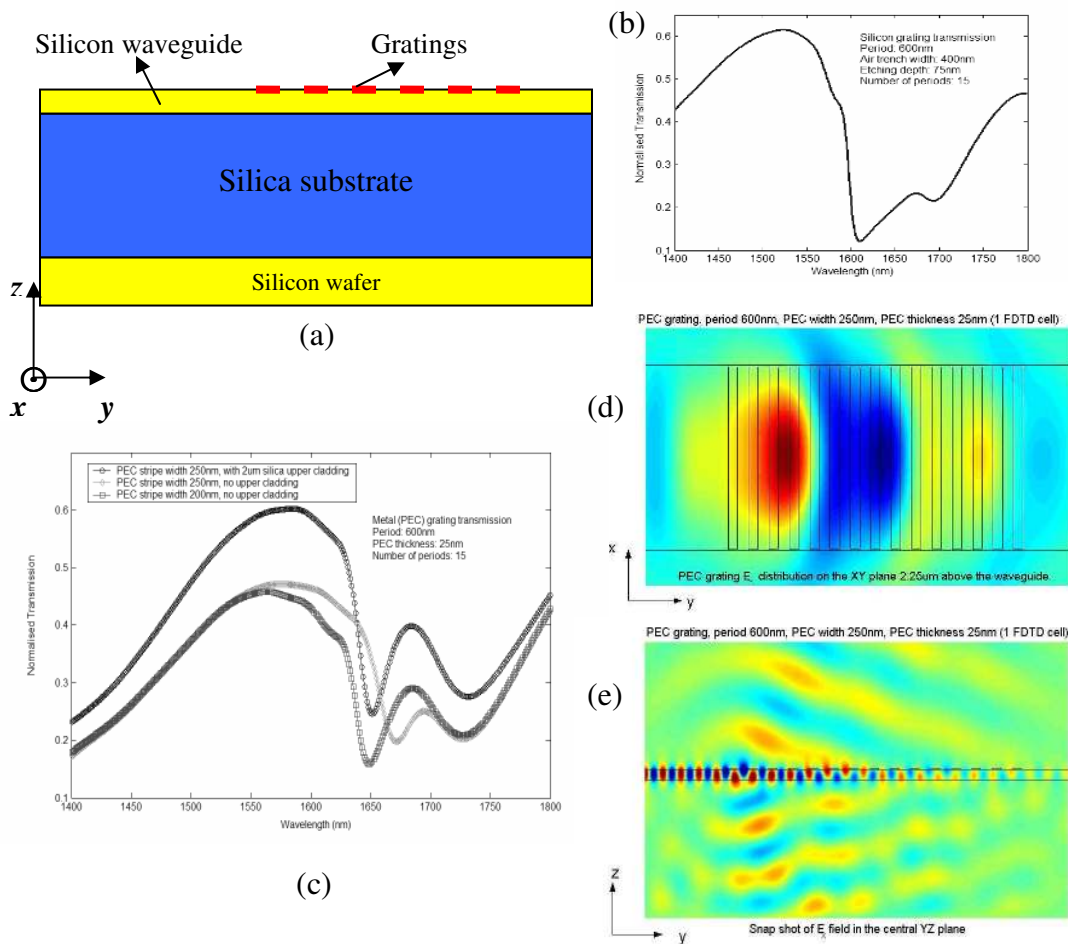

Fig. 2-10 (a) Schematic of the vertical grating coupler. (b) Power transmission of silicon grating coupler. (c) Power transmission of various metal (approximated by PEC) grating couplers. (d) Metal grating vertical transmission snap shot in the XY plane at 1550nm. (d) Metal grating transmission snap shot in the YZ plane at 1550nm.

The results in Fig. 2-10 (b) and (d) show that by adding gratings to silicon waveguide, light can be coupled into free space efficiently (>30% transmission) for a broad wavelength range.

References:

1. K. S. Yee, "Numerical solution of initial boundary value problems involving Maxwell's equations in isotropic media," IEEE Trans. Antennas and Propagation," 14, 302 (1966).
2. A. Taflove, "Computational Electrodynamics: The Finite-Difference Time-Domain Method," second edition, ISBN 1-58053-076-1, Artech House, Boston, MA, 2000.
3. R. Courant, K. Friedrichs, and H. Lewy, "On the Partial Difference Equations of Mathematical Physics," IBM J. 11, 215-234 (1967).
4. M. Qiu, "Computational Methods for the Analysis and Design of Photonic Bandgap Structures," PhD thesis, ISBN 91-7170-640-2, KTH, Sweden, 2000.
5. U. Andersson, "Time-Domain Methods for the Maxwell Equations," PhD thesis, ISBN 91-7283-043-3, KTH, Sweden, 2001.
6. D. Sullivan, "Electromagnetic simulation using the FDTD method," ISBN0-7803-4747-1, IEEE Press, New York, 2000.
7. Min Qiu, F2P http://www.imit.kth.se/info/FOFU/PC/F2P/index.htm
8. B. Strand, U. Andersson, F. Edelvik, J. Edlund, L. Eriksson, S. Hagdahl, and G. Ledfeldt, "GEMS-a Swedish electromagnetic suite of hybrid solvers technical aspects," AP2000 Millennium Conference on Antennas and Propagation, Davos, Switzerland. April 9-14 (2000).
9. Efield AB http://www.efieldsolutions.com/
10. Lucidor cluster http://schelly.pdc.kth.se/pdc/systems_support/computers/lucidor/
11. U. Andersson, "Yee bench - A PDC benchmark code," TRITA-PDC 2002:1, ISRN KTH/PDC/R-02/1, KTH, Sweden, 2002.
12. S. Noda, A. Chutinan and M. Imada, "Trapping and emission of photons by a single defect in a photonic bandgap structure," Nature 407, 608 (2000).
13. B. S. Song, S. Noda and T. Asano, "Photonic Devices Based on In-Plane Hetero Photonic Crystals," Science 300, 1537 (2003).
14. A. Chutinan, M. Mochizuki, M. Imada and S. Noda, "Surface-emitting channel drop filters using single defects in two-dimensional photonic crystal slabs," Appl. Phys. Lett. 79, 2690 (2001).
15. B. K. Min, J. E. Kim and H. Y. Park, "High-efficiency Surface-emitting channel drop filters in two-dimensional photonic crystal slabs," Appl. Phys. Lett. 86, 11106 (2005).
16. S. Fan, Pierre R. Villeneuve, and J. D. Joannopoulos, "Channel Drop Tunneling through Localized States," Phys. Rev. Lett. 80, 960 (1998).
17. C. Manolatou, M. J. Khan, S. Fan, Pierre R. Villeneuve, H. A. Haus and J. D. Joannopoulos, "Coupling of Modes Analysis of Resonant Channel Add-Drop Filters," IEEE J. of Quantum Electron. 35, 1322 (1999).
18. Y. Xu, Y. Li, E. K. Lee and A. Yariv, "Scattering-theory analysis of waveguide-resonator coupling," Phys. Rev. E. 62, 7389 (2000).
19. B. K. Min, J. E. Kim and H. Y. Park, "Channel drop filters using resonant tunnelling processes in two-dimensional triangular lattice photonic crystal slabs," Optics Commun. 237, 59 (2004).

20. K. Hwang and G. Song, "Design of a high-Q channel add-drop multiplexer based on the two-dimensional photonic-crystal membrane structure," Opt. Express **13**, 1948-1957 (2005).

21. M. Qiu and Z. Zhang, "High Q Microcavities in 2D Photonic Crystal Slabs Studied by FDTD Techniques and Pade Approximation," Proc. SPIE. 5733, (2005).

22. W. H. Guo, W. J.　Li, and Y. Z. Huang, "Computation of Resonant Frequencies and Quality Factors of Cavities by FDTD Technique and Pade Approximation," IEEE Microwave Wireless Components Lett. 11, 223 (2001).

23. K. Srinivasan and O. Painter, "Fourier space design of high-Q cavities in standard and compressed hexagonal lattice photonic crystals," Opt. Express 11, 579 (2003).

24. T. Shoji, T. Tsuchizawa, T. Watanabe, K. Yamada, H. Morita, "Low loss mode size converter from 0.3 μm square Si wire waveguides to single mode fibers," Electron. Lett. 38, 1669 (2002).

25. V. Almeida, R. Panepucci, and M. Lipson, "Nanotaper for compact mode conversion," Opt. Lett. 28, 1302 (2002).

26. A. Barkai, "Efficient Mode Converter for Coupling between Fiber and Micrometer Size Silicon Waveguides," The 4th International Conference on Group IV Photonics (GFP 2007).

27. D. Taillaert, P. Bienstman, and R. Baets, "Compact efficient broadband grating coupler for silicon-on-insulator waveguides," Opt. Lett. 29, 2749 (2004).

28. G. Roelkens, D. Van Thourhout, and R. Baets, "High efficiency Silicon-on-Insulator grating coupler based on a poly-Silicon overlay," Opt. Express 14, 11622-11630 (2006).

29. G. Roelkens, D. Van Thourhout, and R. Baet, "High efficiency grating coupler between silicon-on-insulator waveguides and perfectly vertical optical fibers," Opt. Lett. 32, 1495 (2007).

30. S. Scheerlinck, J. Schrauwen, F. Van Laere, D. Taillaert, D. Van Thourhout, and R. Baets, "Efficient, broadband and compact metal grating couplers for silicon-on-insulator waveguides," Opt. Express 15, 9625-9630 (2007).

31. P. Bienstman and R. Baets, "Optical modeling of photonic crystals and VCSEL's using eigenmode expansion and perfectly matched layers," Opt. Quantum Electron. 33, 349-354 (2001).

Chapter 3.   Fabrication

3.1 Overview

As discussed in Chapter 1, silicon photonics has become an important part of integrated photonics. SOI is the key platform for passive PICs. Many fabrication processes can be borrowed from CMOS technology. Leading companies such as Intel and IMEC are developing wafer-scale fabrication process for SOI PICs using only standard CMOS technology. However, many small companies and research institutes are still working on photonic devices on the sample scale, i.e., the wafer must be cleaved into smaller pieces for further processing. Various additional techniques are used, including molecular beam epitaxy (MBE), E-beam lithography, Focused Ion Beam (FIB) etching, and so on.

The fabrication processes are, in short, three steps, as shown in Fig. 3-1. First, materials have to be deposited on the handling wafer. Chemical Vapor Deposition (CVD), MBE, and sputtering are the common deposition techniques. Pattern defining process usually includes photolithography (G-line 436 nm and I-line 365 nm), deep-UV lithography (DUV, 248 or 193 nm), E-beam lithography and Nano Imprint Lithography (NIL). The patterns are created in the polymer layer coated on top. After pattern defining, the sample might be taken back for film deposition again, such as metal sputtering in the lift-off process, or continue into pattern transfer step where various etching techniques take place. The sample can go directly from deposition to pattern transfer via FIB etching, where no hard mask is needed for pattern defining. These three steps might also be repeated for more complicated structures and extra care has to be taken. Alignment marks need to be created during the first iteration and the subsequent patterns will refer to them. Sample surfaces may need to be polished or planarized. Thermal oxidation and annealing might be required in some cases, and so on.
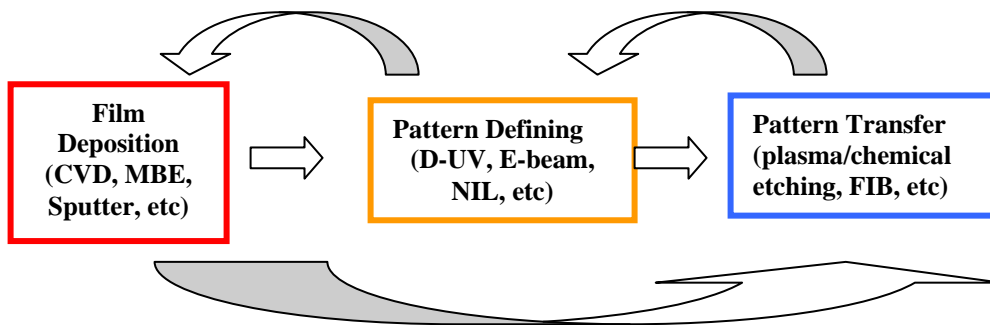

Fig.3-1 Schematic of three-step fabrication process.

In this thesis, plasma enhanced chemical vapor deposition (PECVD) is used to deposit silica buffer layer and hydrogenated amorphous silicon layer on standard 4-in silicon wafers. Though in some cases I-line lithography was used for creating simple waveguides, E-beam is the dominating pattern defining process in my work. Two primary E-beam resist, ZEP520A (positive) and maN 2405 (negative) have been adopted for difference applications. To transfer pattern from resist to silicon, Inductively Coupled Plasma (ICP) dry etching is used. Single resist layer lift-off process has been carried out to transfer metal patterns to the device.

3.2 Plasma enhanced chemical vapor deposition

The machine I have used is STS PECVD, which allows single-wafer (4 inch) plasma deposition of silicon oxide, silicon nitride and amorphous silicon. Technical description is illustrated in Fig. 3-2.

There are many advantages of using PECVD over standard thermal CVDs. It is able to selectively transfer the necessary energy, via plasma, to break the precursors into gas molecules. Deposition can take place at relatively low temperature (~ 300 °C). Thirdly, amorphous silicon has the highest refractive index (3.63) among other common transparent materials at 1550 nm wavelength region. Silica index can be changed easily via germanium doping. The deposited films show good uniformity and surface smoothness [1]. Compared to commercial SOI wafers, the silica buffer and top silicon layer thickness can be flexible using PECVD deposition. Multi-layer structure can be added to form gratings to enhance vertical light confinement [2-3].
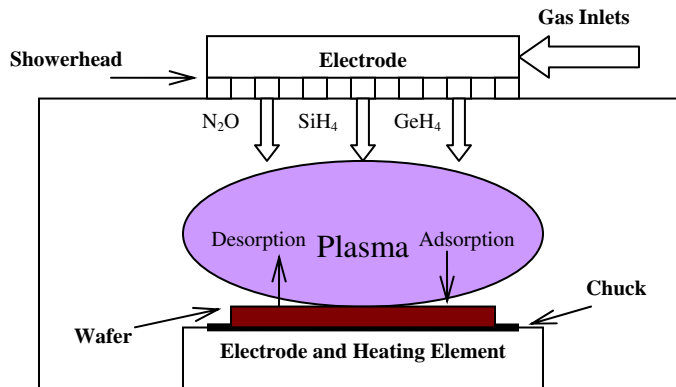
Fig. 3-2 Technical description of PECVD.

For silica deposition, N_2O gas is used for providing oxidizer and SiH_4 for providing silicon. The temperature is set at 300 °C, the ratio between these two gases is optimized at the right RF power. The energy of ion bombardment is controlled at certain range so that it enhances surface mobility of adsorbed radicals, helps H based by-products desorption, and avoids producing point defects or recoil induced disorder in the glass or re-sputtering. The deposition rate can be tuned from 1000 Å/min – 2000 Å/min. The refractive index variation is less than 1.5×10^{-4}. The surface roughness (RMS) measured with AFM (5 µm by 5 µm field) is 3.4 Å [4].

For hydrogenated amorphous silicon (α-Si:H), the amount of hydrogen (provided by SiH_4) is carefully chosen so that it is enough to passivate point defects in the material from unsaturated dangling bonds of silicon in the amorphous network while avoiding generating excessive pores. The deposition rate is around 100 – 120 Å/min. The refractive index variation is less than 1.0×10^{-3}. RMS of surface roughness is 7.5 Å for 250 °C and 6 Å for 300 °C [4].

3.3 E-beam lithography

3.3.1 Introduction

E-beam lithography uses high-energy (1 kV ~ 100 kV) electron beams to generate patterns in a thin (50 nm ~ 1000 nm) polymer layer. The key advantage over photolithography (DUV) is that it beats the diffraction limit of light and is able to make features in the nanometer regime (recall that in Chapter 1, the de Broglie wavelength of a 10 keV electron is roughly 12.3 pm). E-beam lithography has found wide usage in making high-precision masks for photolithography, low-volume production of semiconductor components, and various research applications. Though multiple-source E-beam system has been realized to speed up the exposure process [5-6], it is still not suitable for high-volume manufacturing. The beam must scan, in a serial manner, across the surface to generate patterns.

Many issues affect the resolution of E-beam lithography, including the system issues such as electron beam width, accelerating voltage, working distance, and e-beam resist issues such as sensitivity, contrast and process stability. For most resists, it is difficult to go below 25 nm lines and spaces, and a limit of 20 nm lines and spaces has been found [7].

There are two major problems with E-beam lithography, i.e., stitch error and proximity effect. To understand stitch errors, the e-beam deflection system must be introduced first. In the system column, the electron beam is controlled and deflected by a series of magnetic coils and electrostatic elements, i.e., the electron optics. For each magnification used during exposure, there is a certain area called the write-field. Inside one write field, e-beam can cover the whole area by changing only the electron optics without moving the stage. The deflection has always some errors. Write-filed alignment is a very central adjustment in the process of getting the best possible e-beam lithographic result. It is the adjustment of the electron optics inside the column to the high precision X-Y-Z laser-controlled stage. The stage is considered to be "correct" and the e-beam deflection system is aligned to it. Very often the pattern is large and has to be divided into several write-fields. This is called the stitching of write-fields. It gives rise to stitch errors since there is no perfect matching between adjacent write-fields. These errors can be minimized by careful write-field alignment, increasing junction pattern areas and including over-exposed patches. However, there is no guarantee that stitch errors would be eliminated each time. In most cases, stitch error is caused by the random precision errors when the laser-controlled stage moves. Depending on the working condition, this error can cause pattern mismatch ranging from a few to hundreds of nanometers.

The electron scattering process is introduced to understand the proximity effect. When electron beam is incident on a material, the electrons are scattered both elastically (with angle changes but no energy loss) and in-elastically (with energy loss) [8]. The elastically scattered electrons usually travel a long distance before being absorbed. Those heading backward during elastic scattering are called the back-scattered electrons. The in-elastically scattered electrons can generate X-rays, secondary electrons, Auger

electrons, and etc, depending on their energy loss quanta. The range of the back-scattered electrons is usually much larger than the range of the secondary or Auger electrons. The broadening of beam spot size due to back-scattering in the e-beam resist layer is called proximity effect. It often causes deformed exposed features compared to their fine designed counterparts. Proximity compensation refers to the correction of e-beam exposure dose in densely patterned regions compared to isolated features. Many e-beam systems provide proximity compensation in their software package. These pre-defined correction packages usually have very limited applications since the proximity effect is decided by a variety of factors, such as electron accelerating voltage, resist properties and thickness, substrate materials and thickness, and etc. Very often manual dose adjustment is carried out by trial and error.

3.3.2 E-beam process for photonic crystal surface cavity

Raith Turnkey 150 (Ver. 3.7) SEM & E-beam lithography system is used for E-beam exposure. It is a combination of a SEM manufactured by LEO Electron microscopy Ltd. (now acquired by Zeiss) using the Gemini column and a high precision laser interferometric stage combined with special digital-to-analog converters for the e-beam deflection during lithography, both made by Raith GmbH. The maximum accelerating voltage is 30 kV (25 KV in practice due to previous system failure).
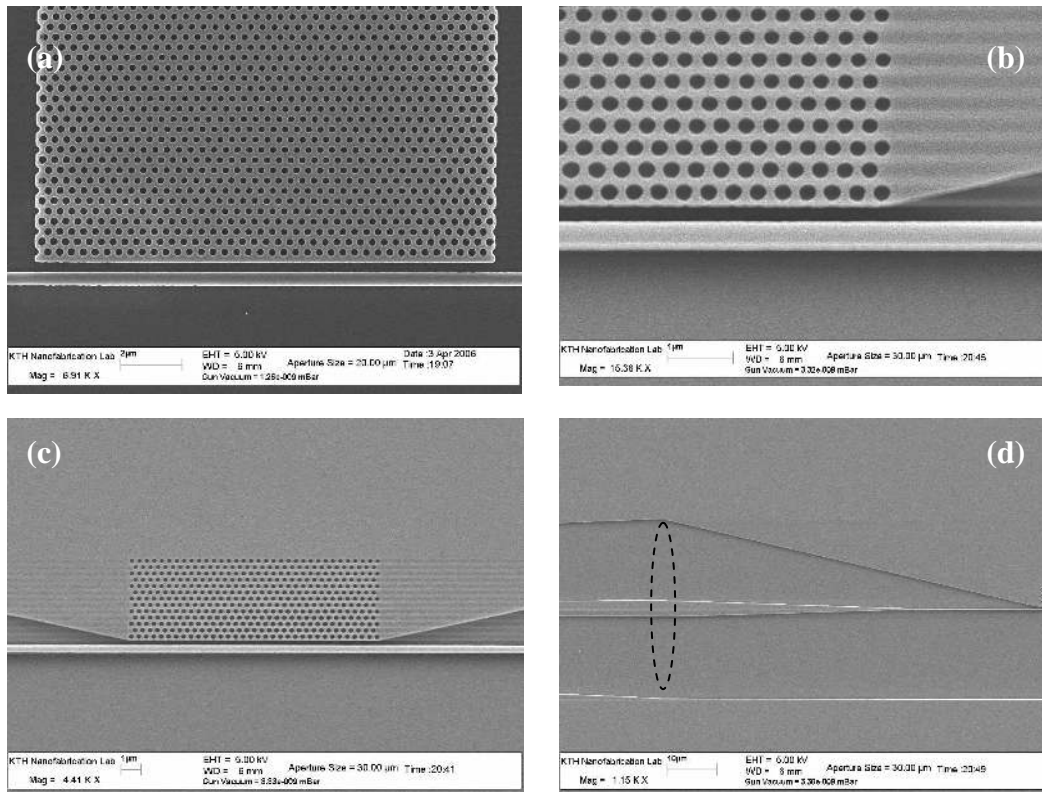

Fig. 3-3 (a)-(c) SEM photos of 2D PhC surface cavity side coupled to a silicon wire waveguide. (d) Tapered access waveguide at the write-field interface (inside the dashed ellipsoid). The stitch error is barely noticeable.

There are two types of e-beam resist. Positive resist undergoes chain-scission upon e-beam exposure and the exposed part becomes soluble. Negative resist reacts to electrons by cross-linking and becomes insoluble after exposure. Positive resist ZEP520A is used for making photonic crystal related devices and negative resist maN 2405 is used for making ring resonator related devices.

Fig. 3-3 (a)-(c) shows the SEM photos of 2D PhC surface cavity side-coupled to a silicon wire waveguide. The proximity effect in the PhC area is corrected manually to reach a relatively uniformed air-hole size. Fig. 3-3 (c) shows the access waveguide at the write-field interface. By careful write-field alignment and applying patches, the stitch error is barely noticeable. The sample is fabricated using ZEP520A. Some key parameters include: 220 nm diameter air hole size, 200 nm wide air gap between silicon waveguide and PhC, 180 nm distance between the PhC edge and the center of the first row of air holes, and etc.

A check-list for exposing photonic crystal related devices using ZEP520A is as follows:

1. Adjust the spin speed and coat the sample with 450 nm - 500 nm undiluted ZEP520A.
2. Bake at 180 °C for 10 min.
3. Set accelerating voltage at 25 kV. Adjust aperture alignment, stigmation and focus for 10 μm and 20 μm apertures.
4. Choose 100 μm write-field size and 20 μm aperture for access waveguides. Choose 170 μm write-field size and 10 μm aperture for central part including PhC cavity and tapered waveguides. Do write-field alignment carefully.
5. Choose area scan mode for all and set step size to 0.006 μm.
6. Measure the current at 10 μm and 20 μm apertures. Set the dose to 60 μC/cm^2 for access waveguides and larger values (depending on the desired hole size) for the PhC pattern.
7. Use macros in the position list to change write-field size (magnification) and aperture combination automatically during exposure.
8. Develop in Pxylen for 1 min 40 s. Rinse in IPA for 30 s.

3.3.3 E-beam process for SOI ring resonators

Fig. 3-4 shows the SEM photos of various ring resonators coupled to silicon wire waveguides. The key issue is to use single pixel line scan in circular mode when exposing the ring-resonator parts. If area scan is chosen, the ring is broken down into small triangular meshes during exposure. This gives bad stair-casing effect on the edges and may leave some blank gaps in the ring region instead of filling it completely. The developing time has to be optimized to fully develop the exposed sample and make sure that the air-gap (60 nm – 140 nm wide) between ring/waveguide, ring/ring is completely opened. The proximity effect in the ring/waveguide, ring/ring coupling region is not serious. There is slight broadening of the waveguide and ring width. It can be further optimized by changing the individual circular line exposure dose.

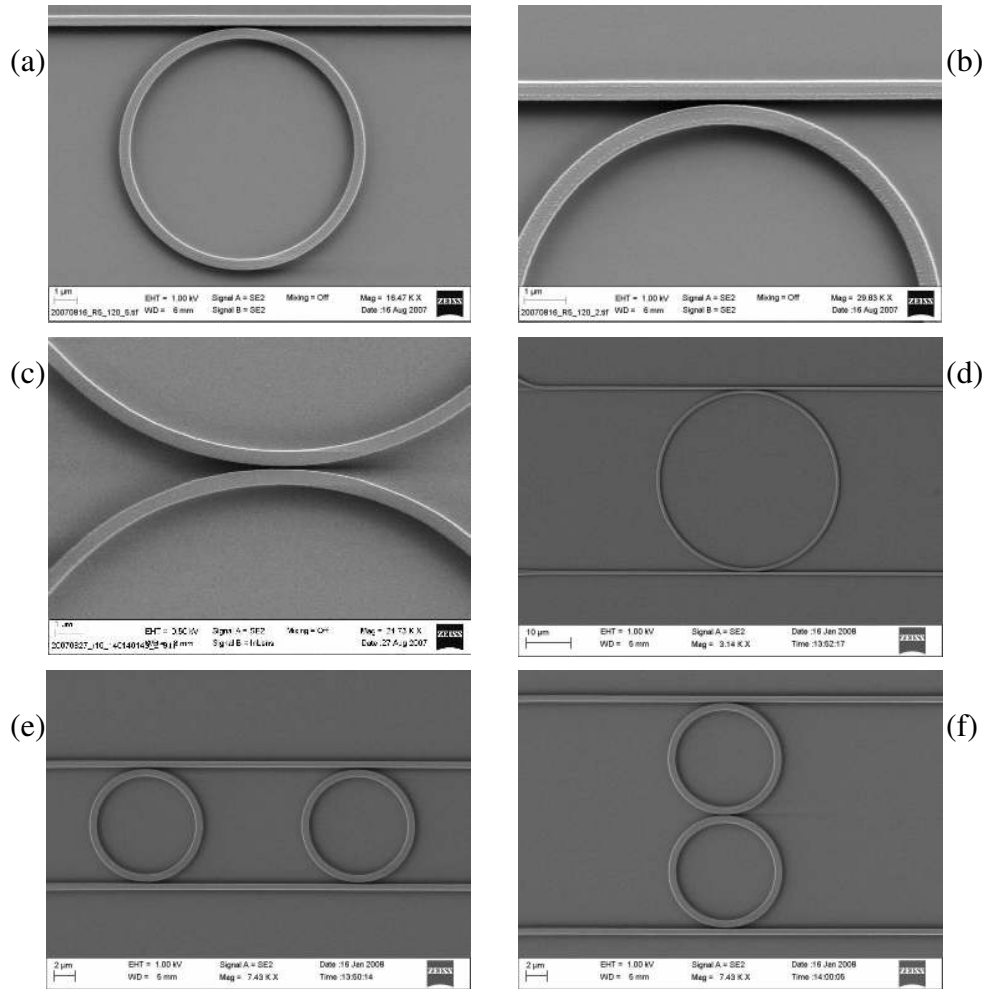A check-list for exposing ring resonator related devices using negative E-beam resist maN 2405 is as follows:

Fig. 3-4 SEM photos of ring resonator related devices. (a)-(b) one 5-µm-radius ring, air gap 120 nm, side coupled to a single silicon wire. (c) two coupled 10-µm-radius rings. (d)-(f) rings between two waveguides.

1. Adjust the spin speed and coat the sample with 350 nm - 400 nm undiluted maN 2405.
2. Bake at 90 °C for 1 min 30s.
3. Set accelerating voltage at 25 kV. Adjust aperture alignment, stigmation and focus for 10 µm and 20 µm apertures.
4. Choose 100 µm write-field size and 20 µm aperture for access waveguides. Choose 350 µm write-field size and 10 µm aperture for central part including rings and tapered waveguides. Do write-field alignment carefully.
5. The access waveguides may be skipped, as discussed later in vertical fiber grating measurement. The whole device can be contained in a single 350 µm write-field.
6. Choose area scan mode for access and tapered waveguides. Choose line scan mode for rings. Set step size to 0.012 µm for all.

7. Measure the current at 10 μm and 20 μm apertures, respectively. Set the dose to 60 μC/cm^2 for access waveguides and larger values for rings and thin waveguides (depending on the desired ring or silicon wire width).
8. Use macros in the position list to change write-field size (magnification) and aperture combination automatically during exposure.
9. Develop in maD 532 for 1 min 20s – 1 min 50 s (depending on the minimum air-gap width). Rinse in water for 30 s.

3.3.4 E-beam process for gold gratings

To couple light efficiently from SMF to silicon waveguide, gold gratings are added to both ends of waveguides [9]. Since the gold stripe width is larger than 200 nm in most cases, single layer resist (ZEP520A) lift-off process is adopted without generating "spikes" attached to the stripe. When the stripe width goes down below 200 nm, double layer resist (PMGI + ZEP520A) has to be used to create desired undercut [10-11]. Fig. 3-5 shows the gratings on top of 10 μm wide waveguides, which must be pre-fabricated using either ZEP520A or maN 2405. On the waveguide sample, there must also be some alignment marks so the position of the waveguides can be fixed during the second exposure. For smooth lift-off, the thickness of the resist layer is recommended to be 10 times larger than the metal layer thickness deposited. The gold thickness is around 20 nm and therefore ZEP520A thickness is larger than 200 nm. However, if the ZEP520A layer is too thick, it is difficult to see the alignment marks during the second exposure. Some compromise has to be made.
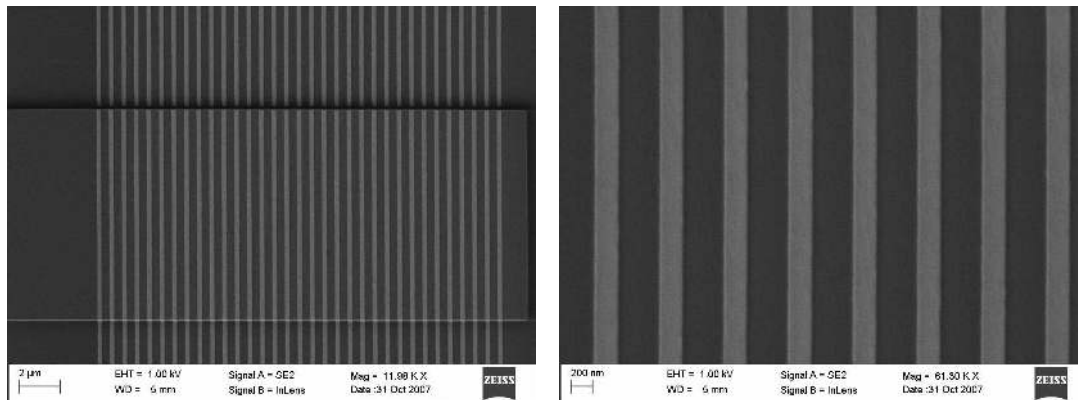

Fig. 3-5 SEM photos gold gratings added to the pre-fabricated waveguide. The period is 600 nm and gold stripe width is 200 nm.

A check-list for exposing grating patterns on pre-fabricated waveguides is as follows:

1. Dilute ZEP520A (1 volume) with Anisol (2 volumes). Adjust the spin speed and make sure the final thickness of ZEP520A is around 200 – 220 nm.
2. Bake at 180 °C for 10 min.
3. Set accelerating voltage at 25 kV. Adjust aperture alignment, stigmation and focus for the 10 μm aperture.
4. Choose 100 μm write-field size. Align the sample using pre-fabricated marks.

5. Choose area scan mode and set step size to 0.006 μm.
6. Measure the current and set the dose to 60 μC/cm^2 for the gratings.
7. The locations of the waveguide ends, where grating patterns are exposed, must be calculated from the alignment marks carefully.
8. Develop in Pxylen for 1 min 30 s. Rinse in IPA for 30 s.

Due to proximity effect, the stripe width after developing is different from the designed values. Table 3-1 lists this discrepancy with respect to different doses. The data are measured under SEM.

Table 3-1 Stripe width changes due to E-beam proximity effect. The grating period is fixed at 600 nm.

	Dose 50 μC/cm^2	Dose 60 μC/cm^2	Dose 70 μC/cm^2	Dose 80 μC/cm^2
Designed width 100 nm	120 nm	125 nm	125 nm	130 nm
Designed width 150 nm	170 nm	185 nm	185 nm	190 nm
Designed width 200 nm	225 nm	240 nm	240 nm	250 nm
Designed width 250 nm	290 nm	300 nm	300 nm	310 nm
Designed width 300 nm	325 nm	330 nm	340 nm	355 nm

3.3.5 Other issues

Other issues in E-beam lithography include:

Resist adhesion problems: The resist may slip off from the substrate during developing. To improve the adhesion, the sample surface must be thoroughly cleaned before spin-coating. A hot 7-up bath is recommended. A mono HMDS film can be applied to improve resist adhesion. However, for ZEP520A the baking temperature is 180 °C. This high temperature may destroy the HMDS film. One solution is to reduce the resist thickness, but this may cause problems in the etching process. The selectivity of ZEP520A to silicon etching is roughly 1:1 and the resist cannot be too thin when used as the etching mask. Another solution is to bake the sample right after exposure but before developing. Post-exposure bake is not included in the standard process of ZEP520A and the dose has to be varied according to the post-exposure baking temperature and time. When developing inverse nano taper couplers, the tip size is below 100 nm. We adopted post-exposure baking at 165°C for 5 minutes. The adhesion is much improved and the tip size is maintained.

Exposure sequence problems: E-beam is sequential scan lithography. It is important to define the exposure sequence explicitly to avoid certain problems. For example, the

exposure of rings must follow immediately after the adjacent waveguides. Otherwise the air-gap width is hard to control due to stage drifting, current drifting and pattern shifting problems. The sequence is automatically generated according to the order the pattern is created in the design file (gds or csf format). However, when the pattern gets complicated, one may lose track of the sequence and have to modify them all together.

Random errors in pattern generators: Sometimes when using large write-field size (350 μm, for example), the patterns may have gaps between them after exposure and developing. Usually the scan precision is high within the write-field and stitch errors only occur between two write-fields. However, when dealing with triangular (such as tapered waveguide) or other irregular shaped patterns using area scan, the pattern generator breaks down the geometry into small meshes and may sometimes leave blank regions. This issue can be solved by adding compensation patches or overlapping the scan regions.

Resist thickness variations: The spin curve provided in the resist manual can be a good starting point. However, the solvent in the resist bottle evaporates gradually and if the spin speed is kept the same, the resist thickness increases over time. It is recommended that the spin-curve should be checked and adjusted every month.

3.4 Plasma etching of silicon

Most dry-etching related to my work is done by the inductively coupled plasma etching (ICP) machine from STS. It is well-suited for deep reactive ion etching (DRIE) of silicon, silicon carbide, and silicon oxide. Since the devices are fabricated in SOI and the top silicon layer is only 250 nm, we simply use E-beam resist (ZEP520A and maN 2405) as the protecting mask to transfer patterns.

To achieve anisotropic etching of silicon and straight sidewalls, SF_6 and C_4F_8 are chosen as plasma source gases [12]. SF_6 is the primary etchant and C_4F_8 provides sidewall passivation by dissociating in the plasma to form CF_x monomers that then polymerize to form fluorocarbon polymers. This polymer deposition results in higher resist selectivity. The etching process is similar to the Advanced Silicon Etch process developed by STS [13]. Increased ion energy in the vertical direction removes the polymer passivation layer faster on the surfaces parallel to the wafer surface. Following selective polymer removal, the silicon surfaces are exposed to reactive fluorine radicals that isotropically etch the unprotected silicon. The remaining fluorocarbon polymer protects the vertical walls from etching. To obtain an optimum profile, SF_6 flow is fixed at 10 sccm and C_4F_8 flow varies from 25 sccm to 30 sccm depending on the chamber condition.

Note that in small trenches or air holes, the etching rate is significantly smaller than in the large openings. This is caused by the reduced rate in the supply of etching species as well as the reduced rate in by-products desorption. Usually the etching time to completely remove the top silicon layer on a dummy sample is recorded. The actual etching time is then adjusted according to the pattern structures. In the photonic crystal related device,

when the air holes are fully etched, the access waveguide is often over-etched. Increasing the C_4F_8 flow level helps alleviate this problem.

Before etching takes place, there may be some resist residues left in the openings, especially when HMDS adhesive layer is deposited. It is better to clean the sample with low-power O_2 plasma. This also helps reduce the roughness in the resist side walls for a better profile. Pre-etching bake is recommended for improvement in the etching selectivity of the resist.

After etching, the remnant of resist is ashed way by high power O_2 plasma followed by 7-up hot bath cleaning. To further reduce the surface roughness, the sample can go through thermal oxidation, where a 20 Å – 50 Å thin silica layer helps smoothen out silicon surfaces [14].

3.5 Metallization and lift-off process

Balzer BAK 600 electron beam evaporation system is used to deposit metal layer for grating couplers. A focused electron beam is used to bombard and vaporize the metal in the chamber and the metal atoms are ionized by arc discharge. Since the desired grating thickness is only 20 – 40 nm, the deposition rate is controlled at 1 Å/s. Gold is chosen as the primary metal because it is relatively easy to achieve smooth thin layers without clustering problems. To improve the adhesion of gold on silicon or silica substrate, 1 – 2 nm titanium layer is deposited first.

The lift-off process is described as follows.

1. Use e-beam lithography to define the pattern, as described in Section 3.3.4.
2. Clean the sample with low-power plasma.
3. Metal evaporation, 1 nm Ti + 20 nm Au.
4. Soak the sample in acetone for 2 minutes with ultrasonic.
5. Soak the sample in resist remover (NMP) for 3 minutes with ultrasonic.
6. Rinse the sample in water for 2 minutes
7. Rinse the sample in IPA for 2 minutes with ultrasonic. Blow dry with N_2.

As discussed earlier, the thickness of e-beam resist (ZEP520A) should be 10 times larger than the metal film deposited. The resist is then easily lifted off in step 4. If the resist layer is not sufficiently thick, the soaking time in step 5 has to be increased and the remover may have to be heated to 50-60 °C. The metal particles can contaminate the sample and once dried it is extremely difficult to remove. Therefore, the sample must be cleaned thoroughly in step 6 and 7.

References:

1. M. Dainese, "Plasma Assisted Technology for Si-based Photonic Integrated Circuits," PhD thesis, ISRN 0348-4467, KTH, Sweden, 2005.

2. C. Symonds, J. Dion, I. Sagnes, M. Dainese, M. Strassner, L. Leroy, and J. L. Oudar, "High performance 1.55 µm vertical external cavity surface emitting laser with broadband integrated dielectric-metal mirror," Electron. Lett. 40, 734-735 (2004).
3. S. Lo, M. Wang, C. Chen, "Semiconductor hollow optical waveguides formed by omni-directional reflectors," Opt. Express 12, 6589 (2004).
4. Dr. Matteo Dainese and Lech Wosinski have worked years in developing high quality PECVD deposition techniques. I have used their recipes for depositing silica and α-Si:H. The characterization data were given by Dr. Matteo Dainese. See Ref. [1] for more details.
5. T. H. P. Chang, M. Mankos, K. Y. Lee, and L. P. Muray, "Multiple electron-beam lithography," Microelectronic Engineering 57, 117-135 (2001).
6. A. Tseng, K. Chen, C. D. Chen, and K. J. Ma, "Electron Beam Lithography in Nanoscale Fabrication: Recent Development," IEEE Transactions on Packaging Manufacturing, 26, 114 (2003).
7. J. A. Liddle, G. M. Gallatin and L. E. Ocola, "Resist Requirements and Limitations for Nanoscale Electron-Beam Patterning," Mat. Res. Soc. Symp. Proc. 739 (19): 19-30 (2003).
8. SPIE Handbook of Microlithography, Micromachining and Microfabrication Volume 1: Microlithography, Chapter 2 Electron Beam Lithography.
9. S. Scheerlinck, J. Schrauwen, F. Van Laere, D. Taillaert, D. Van Thourhout, and R. Baets, "Efficient, broadband and compact metal grating couplers for silicon-on-insulator waveguides," Opt. Express 15, 9625-9630 (2007).
10. J. Walter, "Pulse and Hold Switching Current Readout of Superconducting Quantum Circuits," PhD thesis, ISBN 91-7178-462-4, KTH, Sweden (2006).
11. S. Corlevi, "Quantum effects in nanoscale Josephson junction circuits," PhD thesis, ISBN 91-7178-353-9, KTH, Sweden (2006).
12. The etching recipe was initially developed by Dr. Matteo Dainese.
13. H. Ashraf and J. K. Bhardwaj, "Advanced silicon etching using high density plasmas," SPIE, 2639, 224-233 (1995).
14. S. J. McNab, N. Moll, and Yu. A. Vlasov, "Ultra-low loss photonic integrated circuit with membrane-type photonic crystal waveguides," Opt. Express 11, 2927–2939 (2003).
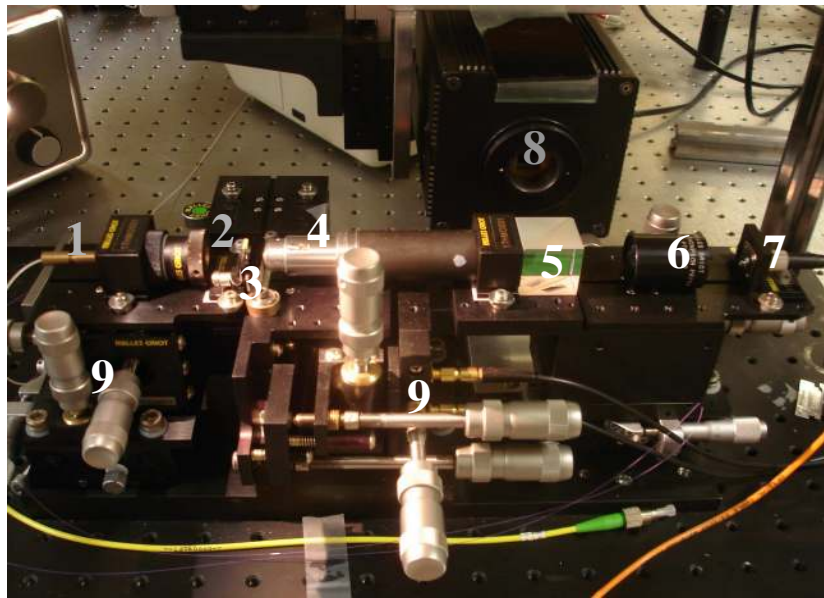
Chapter 4 Characterisation

4.1 Overview

During the fabrication processes, many characterisation techniques are used to measure the device feature size. Typically thin film interferometer (Leitz MPV-SP) and prism coupler are used to characterise the layer (Si or SiO_2) thickness and refractive index from PECVD deposition. Surface profiler (Tencor-P10) is used to determine the resist thickness, material etching depth and metal deposition thickness. SEM (Zeiss Ultra 55) is constantly used to measure critical dimensions in the device.

In this chapter, I focus on the two techniques for measuring passive optical devices, or more precisely, the two techniques used to inject light from SMF to silicon waveguides.

4.2 Butt-coupling method

The setup of this method is shown in Fig. 4-1.

1.Incoming SMF; 2.GRIN lens; 3.Sample; 4.Objective lens; 5.Beam splitter;
6.Glan-Thompson polarizing prism; 7.Detector fiber; 8.Infred camera; 9. Stages

Fig. 4-1. The setup for butt-coupling characterisation method

Using this method, the sample must be cleaved so that the waveguide cross-sections are exposed on both ends. The GRIN lens focuses the incoming light onto the sample edge. The beam spot size is reduced to ~ 2-3 μm, compared to the mode field diameter of ~ 8 μm from SMF. The output light is collected by a 60×, 0.6NA microscope objective. Part of the beam goes through a Glan-Thompson polarizing prism to select the right polarization. A 63µm-core-diameter multimode fiber is used as a detector fiber to increase the collecting aperture. The beam splitter taps out part of the beam and direct it to an infra red camera. By checking the light spot on the camera, the alignment of the

waveguide and objective is optimized. We can then guarantee that the light collected is passing through the silicon waveguide, not through the silica substrate or silicon handling wafer.

The concept of butt-coupling method is simple; however, it is difficult in practice due to the following reasons.

1. The sample must be cleaved. The silicon co-valent bond is much stronger than in III-V semiconductors. It is difficult to cleave a narrow (< 2 mm) sample piece with good facets on a standard 4 inch wafer which is around 525 μm thick. The wafer has to be thinned down, i.e., by CMP, and the waveguide has to be sufficiently long to ensure a good cleaving.
2. Stitch errors in E-beam lithography. Since we lack a modern photolithography tool, such as DUV, we have to resort to E-beam to write the silicon waveguide if the width is below 450 nm. As discussed in Section 3.3.1, the stitch errors can create junction deformation in the waveguide between two write-fields. The waveguide cannot be made too long, usually < 5 mm. This again raises problem in cleaving.
3. The loss is high. Without any sample, the system loss is around 15 – 20 dB. From the simulations in Section 2.4.1, the butt-coupling loss from SMF to silicon waveguide is around 15-20 dB at one facet. With the help of tapered waveguide and focused beam spot, this loss can be reduced. Nevertheless, the typical fiber-to-fiber loss measured for a 2 mm waveguide sample is around 45-55dB. High power input light source has to be used to make sure that output signal goes above the noise level ~ 65-70 dBm.
4. The adjustment is time-consuming. Depending on the quality of the cleaved facets and the orientation of the sample glued to the stage, the adjustment time for optimal output power can take one or two hours. During the alignment, the positions of the stages and the distance between GRIN lens – sample – objective lens has to be adjusted iteratively.
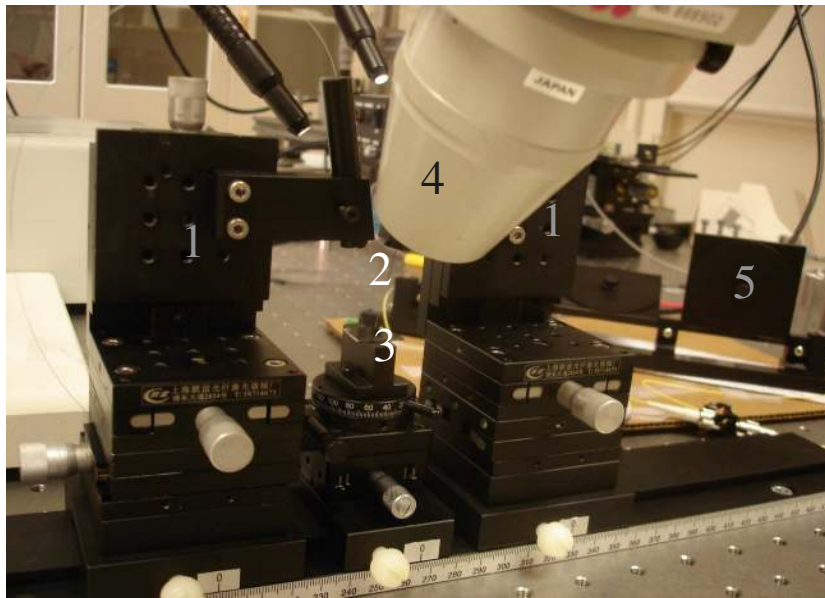
4.2 Vertical fiber-grating coupling method

The setup of this method is shown in Fig. 4-2. A SMF cable is stripped of its coating and cleaved to form a fiber probe. The two probes are placed 10º off the sample normal plane in order to avoid interference between the fiber facet and the sample surface. Under a simple 30× or 40× stereomicroscope, the two probes are centered on the grating areas and 20-30 μm above the surface. The incoming fiber goes through a polarization control unit to select of TE-polarized light.

The initial motivation for changing the measurement method to vertical fiber-grating coupling system is to improve the coupling efficiency. Later on we have found more merits using this system.

1. The sample needs no cleaving. After the gold gratings are added to both ends of the waveguide, the sample is ready for testing. The method is similar to the probe testing technique used to characterize electronic devices, simple and flexible.

2. Stitch errors in E-beam lithography are avoided. Since the two fiber probes can be brought into close proximity without any interference, there is no need to fabricate long waveguides. The whole device can be confined in one E-beam write field 350 μm by 350 μm, as shown in Fig. 4-3 (a). The stitch problem is avoided.

3. The coupling efficiency is high. From the simulations in Section 2.4.5, the peak transmission is 45%. As shown in Fig. 4-4 (b), we have measured a minimum 17dB fiber-to-fiber loss for a straight 350 μm long, 10 μm wide and 250 nm thick waveguide.

4. The adjustment is fast. Under microscope, the fiber probes are positioned right above the grating areas. This usually takes only a few minutes for optimal position adjustment, plus a few more minutes for polarization adjustment.

1.Fiber holder; 2.Fiber probes; 3.Sample;
4.Micrscope; 5.Polarisation control unit

Fig. 4-2. The setup for vertical fiber-grating coupling method

Fig. 4-3 (a) shows the 4 waveguides and the alignment marks in the 350 μm by 350 μm E-beam write field. The waveguides have the same length of 350 μm. The bottom waveguide has a width of 5 μm and coming up the second waveguide has a width of 10 μm. The third waveguide starts with 10 μm width, goes 25 μm and then the width tapers down to 440 nm over a distance of 100 μm. The 440 nm width silicon wire goes another 100 μm before tapering up the same way. The top waveguide has a width of 2 μm. Gold gratings of period 600 nm and gold stripe width 200 nm, i.e., filling factor 33.3%, are added to all the waveguide ends. The transmission spectra of these four waveguides and a 2 mm long 10 μm wide waveguide are compared in Fig. 4-3 (b).
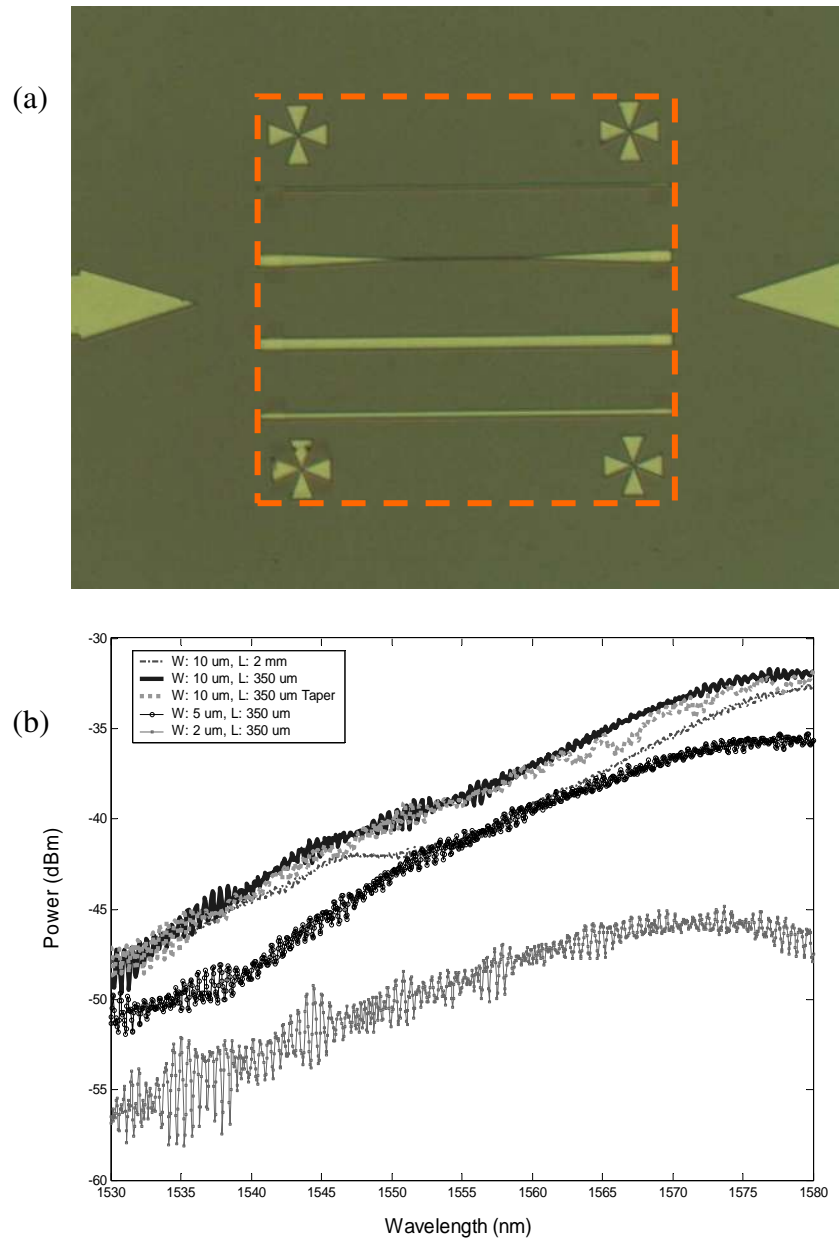
Fig. 4-3 (a) Four waveguides and alignment marks are confined in one E-beam write field, indicated by a dashed box, 350 μm by 350 μm. (b) The transmission spectra of different waveguides.

A few conclusions can be made from Fig. 4-3(b).

1. The incoming light has a power of -15 dBm and this gives the minimum fiber-to-fiber loss of 17 dB at 1577 nm for 10 μm width, 350 μm long waveguide.
2. Extra loss of 2 – 4 dB is introduced when the waveguide width shrinks from 10 μm to 5 μm.
3. Coupling efficiency drops down tremendously if the waveguide width further shrinks

to 2 μm.

4. The tapering loss is barely noticeable.

5. Comparing the waveguide with the same width of 10 μm but different length, 350 μm and 2 mm, there is 1-3 dB difference in the detected power. The waveguide loss is in part due to the material absorption but also due to the scattering at write-field junctions (stitch errors) in E-beam lithography.

6. The coupling efficiency depends on the thickness of the top silicon layer as well as the silica buffer below. In the SOI sample we have worked on, the top silicon thickness is 250 nm and silica buffer thickness is 3 μm. The grating period is 600 nm and gold stripe width is 200 nm, i.e., filling factor 33.3%. For this configuration, the peak transmission occurs around 1575 nm. The 3dB bandwidth of the grating coupler is around 30 – 40 nm. The central coupling wavelength, the coupling efficiency and bandwidth will shift if different SOI wafers and grating couplers are used.

Chapter 5.   Main Results

In Chapter 2, I have selected some important simulation results in my PhD studies. The fabrication processes for some silicon-based photonic devices are introduced in Chapter 3 and the methods for characterising these devices are discussed in Chapter 4. In this chapter, I will summarize some of the main results of my research.

5.1 Photonic crystal surface cavity

It is desirable to combine low-loss dielectric waveguides and high Q photonic crystal cavities. The waveguides are fabricated using standard microelectronic (silicon) technologies and the photonic crystal cavities are placed only locally where necessary. This gives freedom to adjust the coupling between waveguides and cavities continuously via their spacing. On the other hand, a lot of efforts have been made to find high Q cavities that are robust to fabrication imperfections and preferably avoid the fragile membrane structure. Among them surface-mode cavities have attracted much attention.

It has been shown that due to the existence of photonic band gaps, surface waves can exist at the dielectric/air interface of photonic crystals [1-4]. If both ends of the surface edge are terminated by reflecting mirrors a cavity is formed for surface modes that obey Fabry-Perot condition, i.e., the round-trip accumulated phase $\Phi=2kL+2\Delta\phi$ is multiples of 2π, where k is the wave vector, L is the cavity length and $\Delta\phi$ is the phase shift associated with reflection from the boundary. This surface-mode cavity is promising solution, as it avoids fragile membrane structure and can be easily integrated with waveguiding devices using standard SOI technology.

Fig. 5-1 (a) shows the schematic of the surface-mode cavity side coupled to a silicon wire waveguide. The lattice constant a of the PhC is 380nm and the regular air hole diameter of the PhC is 228nm. The scattering loss of reflecting mirrors in the x direction are reduced by slightly enlarging the radius of six surface holes close to the boundary. Fig. 5-1 (b)-(c) shows the results of the parallel 3D FDTD simulations of the surface cavity.

The fabrication procedure involves three major steps. First, low temperature (300°C) plasma enhanced chemical vapor deposition (PECVD) is used to deposit a 6μm thick SiO_2 buffer layer, on top of which a 280nm thick hydrogenated amorphous silicon (a-Si:H) top layer is deposited. Secondly, we use e-beam lithography to write patterns of the photonic crystal slab and the wire waveguide. Great care has been taken to reduce the proximity effect so that the airholes remain uniformly large. After a series of dose tests, the distance between the surface edge and the waveguide is controlled at 200nm. The truncation parameter δ is also fixed at 180nm. In the last step, the pattern is transferred to top silicon layer by ICP etching. The etching recipe is optimized so that the holes are fully etched. Since the etching is done in one step, we have observed some over-etch into the silica layer (around 100nm of depth) in large opening areas, i.e., the opening area to the other side of the waveguide away from PhC. This, however, has little effect on light transmission through the waveguide according to our simulations. SEM photos of the fabricated device can be found in Fig. 3-2 (b)-(d).

After cleaving, the samples were characterized by butt-coupling method. An Erbium doped fiber based ASE source, emitting between 1.52µm and 1.61µm, is used as input. The resolution of the spectrum analyzer is set to 0.2nm and the number of averaging times is 10 to reduce the noise effect. The measured transmission spectrum for the fabricated filter device is shown in Fig. 5-1 (d). The absolute transmission is normalized by the transmission through an identical waveguide without any side coupling. We obtained a distinct transmission dip around 1580nm, which is in good agreement with the design. The system Q is around 600. The extinction ratio is above 10 dB and the intrinsic Q is estimated to be ~2000.
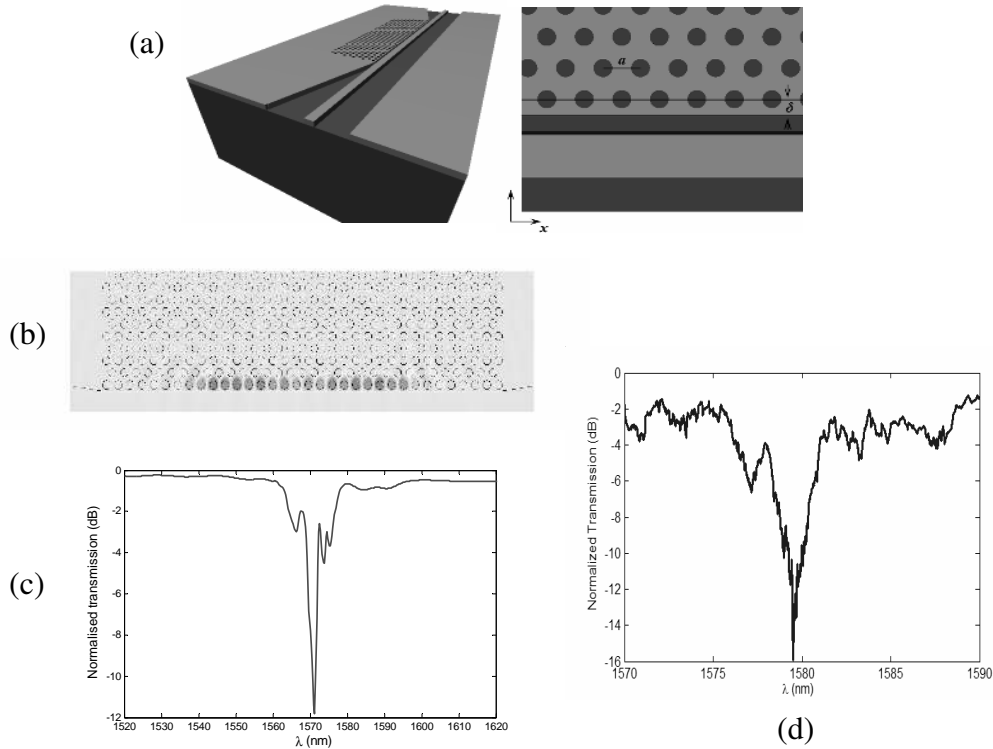

Fig. 5-1 (a) Schematic of photonic crystal surface mode cavity side coupled to silicon wire waveguide in SOI structure. (b) H_z field distribution of the surface mode at central slab plane; (c) simulation result for the power transmission of the optimized filter design. (d) Normalized transmission spectrum for the fabricated device measured from butt-coupling light injecting method.

5.2 Micro-ring resonators

Microring resonators have found wide applications in optical filtering, add-drop multiplexing, dispersion compensation and bio-sensing. In most cases, a high quality factor (Q) and deep notch are desired. Most high Q rings have been demonstrated in single-crystalline SOI structure [5-8]. However, little has been done to investigate the dual-mode splitting and enhanced drop effect by use of concentric rings. In this section, I provide some brief analysis of single-waveguide/ring structure by time-domain coupled mode theory [9-10] and compare the theoretical transmission spectra with those obtained experimentally. Some results of ring resonators on amorphous silicon are shown.

5.2.1 Mutual mode coupling due to sidewall gratings

The schematic is shown in Fig. 5-2. We note from experiments that wave coming from the waveguide generates one of the propagating modes in the ring, which in turn can generate the other counter-propagating mode due to periodic structural roughness. This roughness can be enhanced or eliminated by changing the scan procedure during the E-beam process. To generalize, we include both modes in the coupled mode equations and relate them by mutual coupling coefficient u. For power conservation, u is a real number.
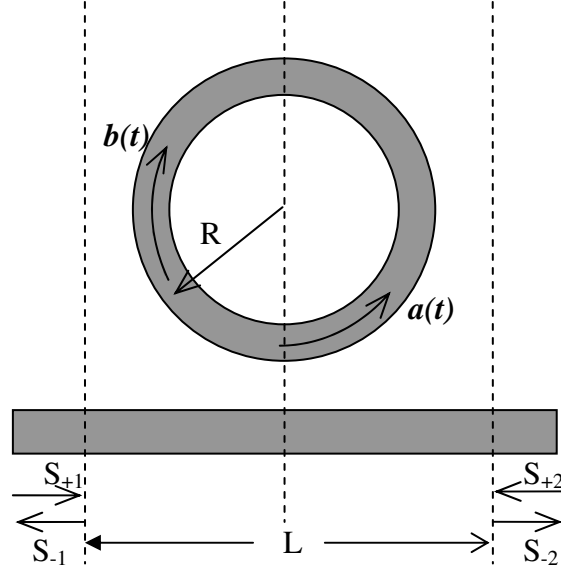

Fig. 5-2 Schematic of a ring resonator side coupled to a waveguide. Wave propagating from left to right (S_{+1}) in the waveguide only generates the counter-clockwise travelling mode $a(t)$ in the ring. Clockwise travelling mode $b(t)$ can be generated by $a(t)$ due to periodic roughness along the ring.

The change rate of the energy stored in the ring resonator for the counter-clockwise traveling mode is given by

$$\frac{da}{dt} = \left(j\omega_a - \frac{1}{\tau_a} \right)a - j\kappa_a S_{+1} - jub \qquad (1)$$

where ω_a is the resonant frequency of the counter-clockwise mode in the ring, τ is the photon life time, κ is the mutual coupling between the ring and the waveguide. The reciprocal of photon life time is the decay rate $1/\tau$, which is related by power coupling to the waveguide ($1/\tau_e$) and power dissipating due to intrinsic losses ($1/\tau_i$). Thus, $1/\tau = 1/\tau_e + 1/\tau_i$. The quality factor (Q) is decided by the photon life time, i.e., $Q = \omega_0\tau/2$. The intrinsic Q and ring/waveguide coupling Q are denoted as Q_i and Q_e, respectively. The waveguide/ring coupling coefficient and the power decay rate are related by $|\kappa|^2 = 2/\tau_e$. Similarly,

$$\frac{db}{dt} = \left(j\omega_b - \frac{1}{\tau_b} \right)a - j\kappa_b S_{+2} - jua \qquad (2)$$

41

Assume the propagation constant in the waveguide is β. The outgoing waves are related by incoming waves by

$$S_{-2} = e^{-j\beta L}(S_{+1} - j\kappa_a^* a) \tag{3}$$

and

$$S_{-1} = e^{-j\beta L}(S_{+2} - j\kappa_b^* b) \tag{4}$$

We study the steady-state solution and assume $e^{j\omega t}$ time dependence for the resonator and waveguide modes. With only input from port 1 and $S_{+2} = 0$, the power of the outgoing wave can be derived from Eq. (1)-(4).

$$|S_{-2}|^2 = |S_{+1}|^2 \left|1 - \frac{|\kappa_a^2| B}{AB + u^2}\right|^2 \tag{5}$$

where

$$A = j(\omega - \omega_a) + \frac{1}{\tau_a} \text{ and } B = j(\omega - \omega_b) + \frac{1}{\tau_b}.$$

The transfer function can be written as

$$T(\omega) = \frac{|S_{-2}|^2}{|S_{+1}|^2} = \left|\frac{D}{C}\right|^2 \tag{6}$$

where $C = AB + u^2$ and $D = C - |\kappa_a^2| B$.

Consider the conventional case when mutual coupling coefficient $u = 0$.

$$T = \left|1 - \frac{|\kappa_a^2|}{A}\right|^2 = \frac{4(\omega - \omega_a)^2 + \left(\dfrac{1}{Q_{ae}} - \dfrac{1}{Q_{ai}}\right)^2}{4(\omega - \omega_a)^2 + \left(\dfrac{1}{Q_{ae}} + \dfrac{1}{Q_{ai}}\right)^2}$$

When the intrinsic Q and coupling Q of mode $a(t)$ become the same, i.e., when $Q_{ae} = Q_{ai}$, T becomes zero at resonant frequency and the channel is completely dropped. This is the conventional critical coupling.

Let's see the case when $u \neq 0$. To simplify the analysis, we assume the two propagating modes $a(t)$ and $b(t)$ are degenerate in the sense that their resonant frequencies and decay rates are the same, thus $A = B$. For complete channel drop, both the real part and imaginary part of D must equal zero.

$$\text{Im}\{D\} = 0 \Rightarrow \omega = \omega_a = \omega_b.$$

$$\text{Re}\{D\} = 0 \Rightarrow u^2 = u_m^2 = \frac{\omega_a \omega_b}{4Q_b}\left(\frac{1}{Q_{ae}} - \frac{1}{Q_{ai}}\right). \tag{7}$$

Since u is a real number, Eq. (7) can only be satisfied when $Q_{ai,} > Q_{ae}$
It is convenient to define a mutual coupling Q factor Q_u. Assume $\omega_a = \omega_b = \omega_0$,

$$Q_u = \frac{\omega_0}{2|u|}.$$

When u = u_m,

$$\frac{1}{Q_{um}^2} = \frac{1}{Q_b}\left(\frac{1}{Q_{ae}} - \frac{1}{Q_{ai}}\right).$$

For $Q_a = Q_b$,

$$\frac{1}{Q_{um}^2} = \frac{1}{Q_{ae}^2} - \frac{1}{Q_{ai}^2}.$$

Note that Q_u is not related to any power loss in the system. It is merely a figure that manifests the mutual coupling rate for the two traveling modes in the ring.

Fig. 5-3 illustrates the transmission properties when $Q_u \to \infty$ (u = 0), $Q_u > Q_m (u^2 < u_m^2)$, $Q_u \approx Q_m (u^2 \approx u_m^2)$ and $Q_u < Q_m (u^2 > u_m^2)$ for the case when $Q_{ai,} > Q_{ae}$ and $A = B$.
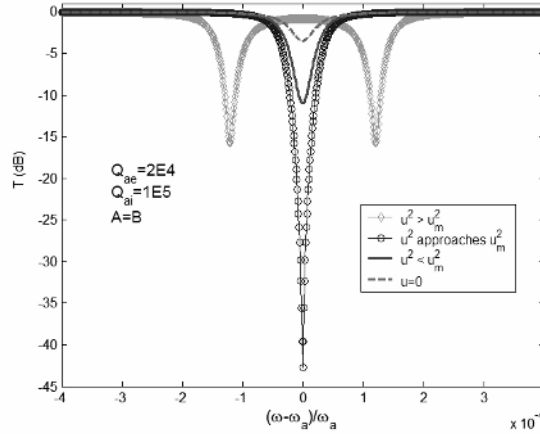

Fig. 5-3 Illustration of the dependence of transmission spectra on the mutual coupling coefficient u. With the presence of mutual coupling, the notch becomes deeper. At optimal coupling u_m, complete channel drop can be reached. When u further increases, mode splitting occurs.

In practice it is difficult to guarantee the conventional critical coupling for complete channel drop. However, with the help of mutual coupling, the notch depth improves and it is possible to reach new critical coupling at u_m. When u further increases, the resonance notch will split into two. This can be a useful feature as it fills the vacant frequency band and more wavelengths can be adopted for operation.

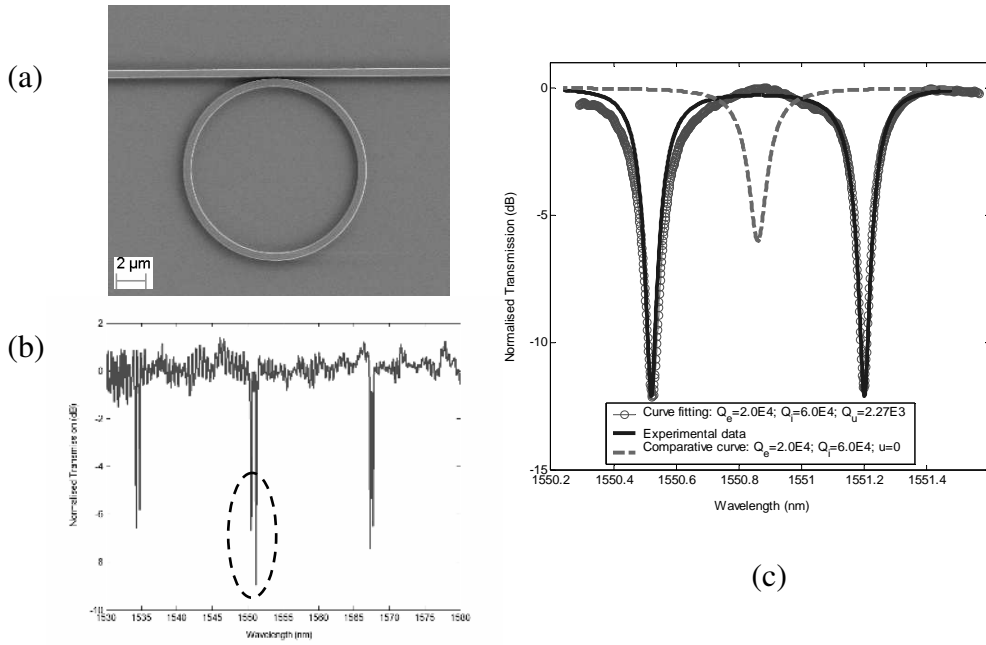Fig. 5-4 shows the SEM photo and measurement results of a 5-µm-radius ring, where obvious mode splitting occurs.

Fig. 5-4 (a) SEM photo of a 5-μm-radius ring. (b) broad spectrum transmission. (c) Curve fitting for one of the notch groups. The intrinsic Q value obtained is 6×10^4 and the coupling Q is 2×10^4. The split notches are deeper than the case without mutual coupling (12dB compared to 6dB).

Fig. 5-5 shows the SEM photo and measurement results of a 10-μm-radius ring. The Q_u value obtained from curve fitting is 1.218×10^4, close to Q_{um} 1.204×10^4, resulting in a notch depth of ~ 40 dB.

Fig. 5-5 (a) SEM photo of a 10-μm-radius ring. (b) broad spectrum transmission. (c) Curve fitting for one of the notch groups. The intrinsic Q value obtained is 1.5×10^5 and the coupling Q is 1.2×10^4. The notch depth is much improved, 40dB compared to the case without mutual coupling where the notch is barely visible.
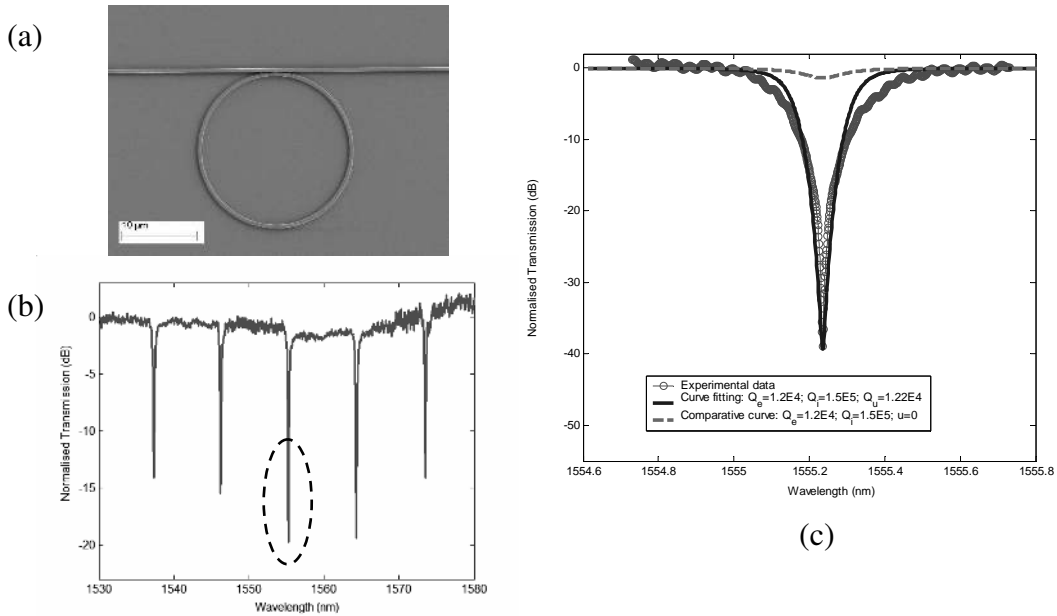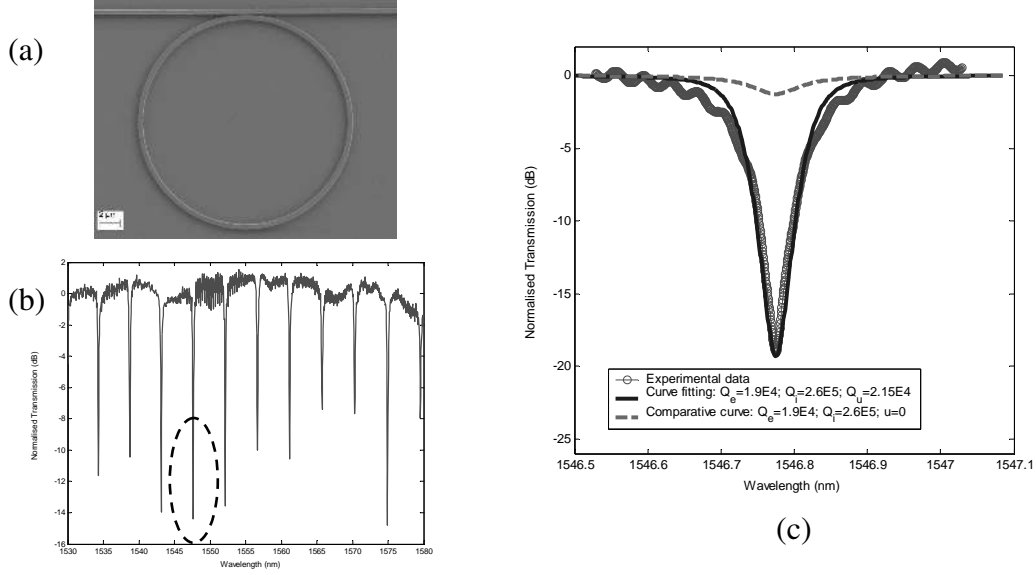
Fig. 5-6 (a) SEM photo of a 20-μm-radius ring. (b) broad spectrum transmission. (c) Curve fitting for one of the notch groups. The intrinsic Q value obtained is 2.6×10^5 and the coupling Q is 1.9×10^4. The obtained Q_u value 2.15×10^4 is larger than Q_{um} 1.91×10^4.

Fig. 5-6 shows the SEM photo and measurement results of a 20-μm-radius ring. The intrinsic Q value goes up to 2.6×10^5.

It is also of importance to calculate the loss per round trip in the micro-ring resonator.

The relative power loss after travel through a full circle is

$$PLR = \exp\left(-\frac{2T}{\tau}\right), \tag{8}$$

where the period T is the time the wave needs to travel through a round trip.

$$T = \frac{2\pi R}{v_g} = \frac{2\pi R n_g}{c}. \tag{9}$$

The group index n_g can be estimated from the free spectrum range (FSR).

$$FSR = \frac{\lambda_0^2}{2\pi R n_g} \tag{10}$$

From (4)-(6), the power loss per round trip is given by

$$PLR = \exp\left(-\frac{2\pi\lambda_0}{Q FSR}\right) \tag{11}$$

45

One can convert PLR in dB scale and then divide it by the perimeter of the ring to obtain loss (dB) per unit length. In Eq. (4) if τ is replace by τ_i, i.e., in Eq. (7) Q replaced by Q_i, one can get the intrinsic loss per round trip in the ring. Take the value from Fig. 5-4, 5-5 and 5-6, the intrinsic loss per unit length in the 5, 10, 20-μm-radius ring is 12.47 dB/cm, 6.24 dB/cm, 2.94 dB/cm, respectively. The results are comparable to those published in [5-8].

We found out the processing cause of the periodic roughness that gives rise to mutual mode coupling in the ring resonator. Basically the pseudo-circular scan mode in E-beam has generated nodes with period around tens to one hundred nanometers. The SEM photos of this periodic roughness on the sidewalls are shown in Fig. 5-7. When the circular scan mode is corrected, we face the difficulty of hitting the conventional critical coupling without the help of mutual mode coupling. Most of the transmission spectra show only shallow notches despite a high intrinsic Q factor.
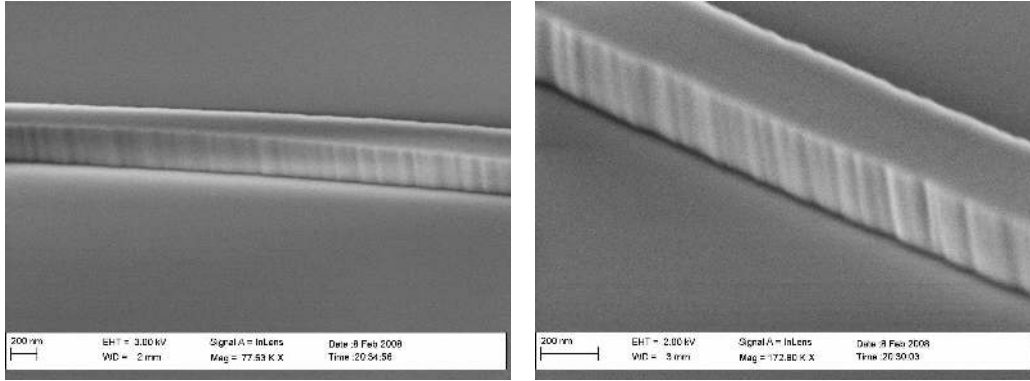

Fig. 5-7 SEM photos of the sidewalls of a 20-μm-radius ring. The periodic roughness is clearly seen.

5.2.2 Concentric rings

We note that the deeper notch is the result of the secondary coupling between ring resonator modes, it is possible to find another solution without the periodic disturbance along the ring. The schematic is shown in Fig. 5-8. A second ring is placed, concentrically, inside the outer-ring. The waveguide/ring, ring/ring separation is set so that the waveguide only couples to the outer-ring. The outer-ring then generates the travelling mode, along the same direction, in the inner-ring.

We redefine u as the mutual inter-ring coupling coefficient. From the same time-domain coupled mode analysis, Eq. (1)-(4) can be re-written as

$$\frac{da}{dt} = \left(j\omega_a - \frac{1}{\tau_a} \right) a - j\kappa_a S_{+1} - jub \qquad (12)$$

$$\frac{db}{dt} = \left(j\omega_b - \frac{1}{\tau_b} \right) a - jua \qquad (13)$$

$$S_{-2} = e^{-j\beta L}(S_{+1} - j\kappa_a^* a) \tag{14}$$
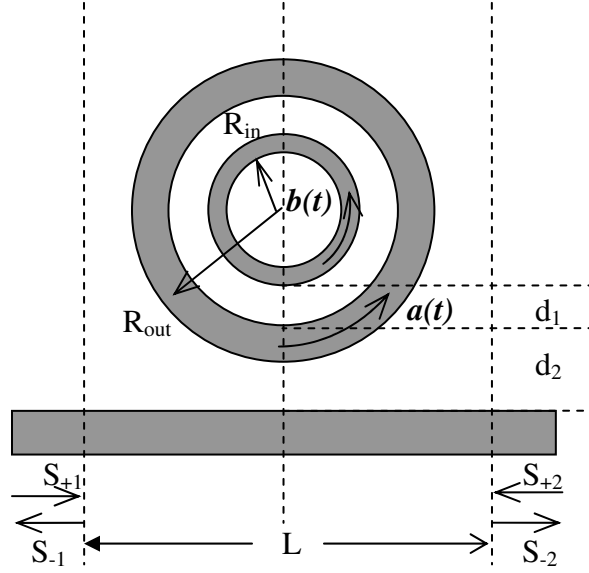
$$S_{-1} = e^{-j\beta L} S_{+2} \tag{15}$$

Fig. 5-8 Schematic of two concentric ring resonators side coupled to a waveguide. Wave propagating from left to right (S_{+1}) in the waveguide only generates the counter-clockwise travelling mode *a(t)* in the outer ring. Counter-clockwise travelling mode *b(t)* in the inner ring can then be generated by evanescent directional coupling from *a(t)*.

Again for steady-state solution we assume $e^{j\omega t}$ time dependence for the resonator and waveguide modes. With only input from port 1, and $S_{+2} = 0$. The solution of the transfer function is exactly the same as the previous case.

$$T(\omega) = \frac{|S_{-2}|^2}{|S_{+1}|^2} = \left|\frac{D}{C}\right|^2 \tag{6}$$

where $A = j(\omega - \omega_a) + \dfrac{1}{\tau_a}$, $B = j(\omega - \omega_b) + \dfrac{1}{\tau_b}$

and $C = AB + u^2$, $D = C - |\kappa_a^2| B$.

In the previous case, it is easy to assume the two counter-propagating modes share the same resonance frequency and decay rates because they exist in the same ring. For the concentric double ring structure, the two modes are intrinsically different. Nevertheless, Consider the situation when the ring radius is much larger than their separation (Rin >> d1), we can still assume A ≈ B to simplify the case. Then the dependence of the transfer function T on the mutual inter ring coupling coefficient *u* is similar to that illustrated in Fig. 5-3.

The magnitude of the mutual inter ring coupling coefficient mainly depends on the perimeters of the rings and the separation width between them. We have experimentally demonstrated the enhancement of notch depth by use of a second ring. The results and SEM photos are shown in Fig. 5-9. The outer ring has a radius of 40 μm. The inner ring radius is 39 μm. The waveguide/ring gap width is 150 nm and the ring/ring gap width is 480 nm. In Fig. 5-9 (d)-(e) the curves were fitted using Eq. (6) assuming $A = B$.

For bio-sensing applications, concentric rings not only increase the modal area for bio-molecule detection, but also hold the potential for enhanced notch depth and thus make it easier for power detection at the output port. Research work on multiple concentric rings is still underway at the moment of this thesis.
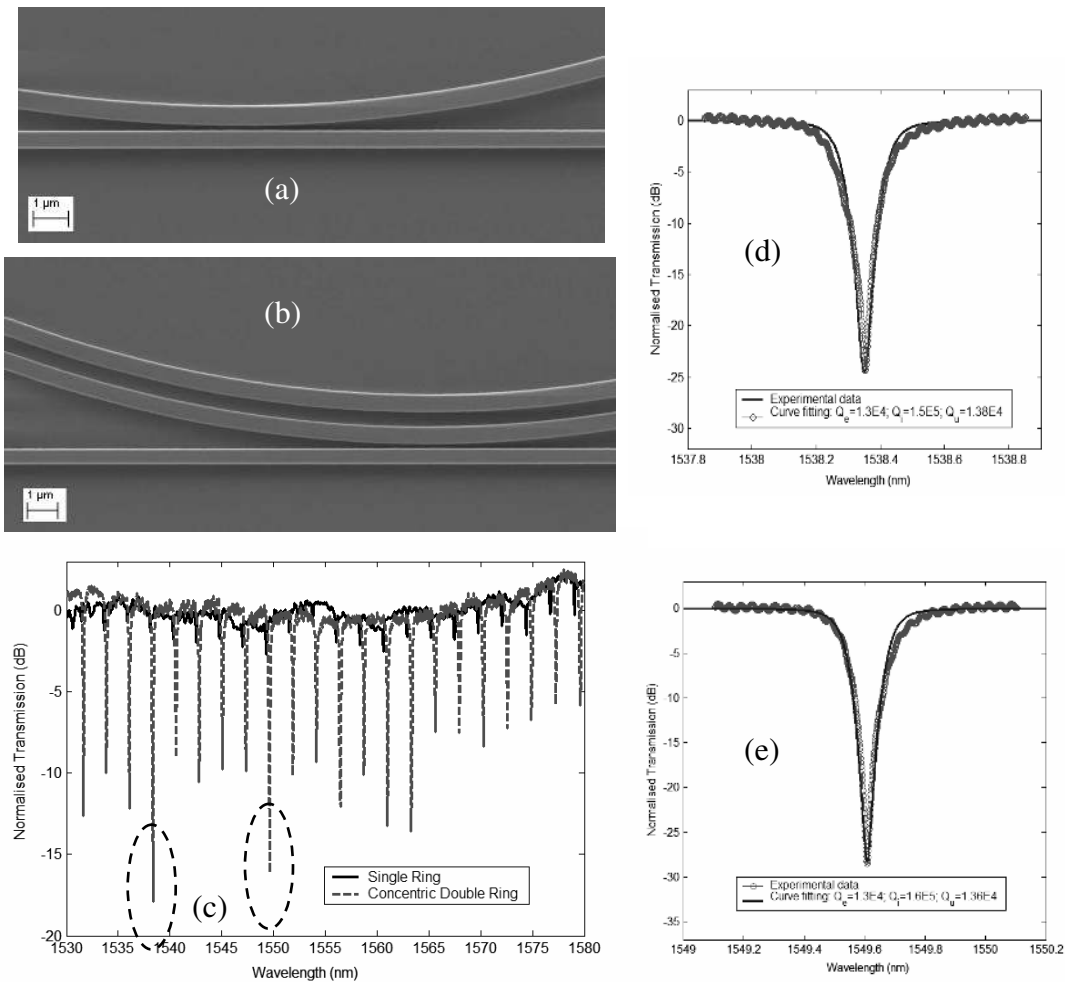
Fig. 5-9 (a) SEM photo of a single 40-μm-radius ring. (b) SEM photo of a dual 40-39-μm-radius ring structure. (c) broad spectrum transmission for both cases. The double ring structure exhibits much enhanced notch depth. (d)-(e) Curve fitting for two of the deep notches.

5.2.3 Micro-rings in amorphous silicon

It is also interesting to see the results of ring resonators in α-Si:H. As discussed before, PECVD is an essential tool in CMOS technology and amorphous silicon provides much cheaper solution than single-crystalline silicon on SOI platform.

SEM photos and measurement results of an α-Si:H ring resonator are shown in Fig. 5-10. The bending radius is 40μm. The ring-width is 400 nm. The width of the air gap between the ring and waveguide is 100nm. The resonance splitting and deep notches indicate the presence of mutual mode coupling. The estimated intrinsic Q value for the notch in Fig. 5-10(c) is 5.6×10^4.
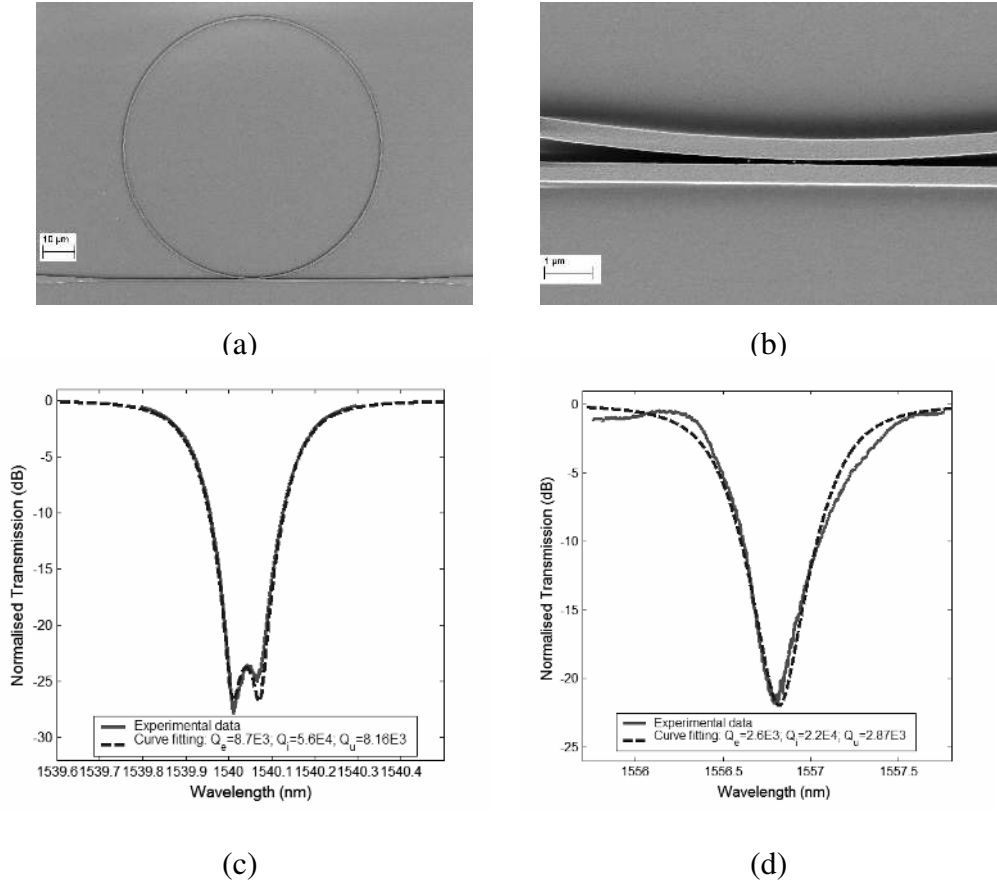

(a)   (b)

(c)   (d)

Fig. 5-10 (a)-(b) SEM photos of the α-Si:H microring resonator with bending radius 40 μm and air gap width 100 nm. The waveguide/ring width is 400 nm and thickness is 250 nm. (c)-(d) Measured transmission spectra verses fitted curves .

To make a comparison, we have fabricated and analyzed the device of the same lateral and vertical geometry in the single crystalline silicon sample. The fabrication process is the same. The results are shown in Fig. 5-11. The best notch occurs at 1574.6 nm with intrinsic Q estimated as 9.1×10^4.

Note that the intrinsic Q values of α-Si:H and single-crystalline silicon ring resonators are on the same order of magnitude. Using Eq. (11) we have calculated the loss per unit length for both samples. For α-Si:H, the loss is 15.30 dB/cm and for single-crystalline silicon the loss is 9.16 dB/cm. The two loss figures are comparable and we believe that α-Si:H is a promising candidate platform for high quality optical devices.
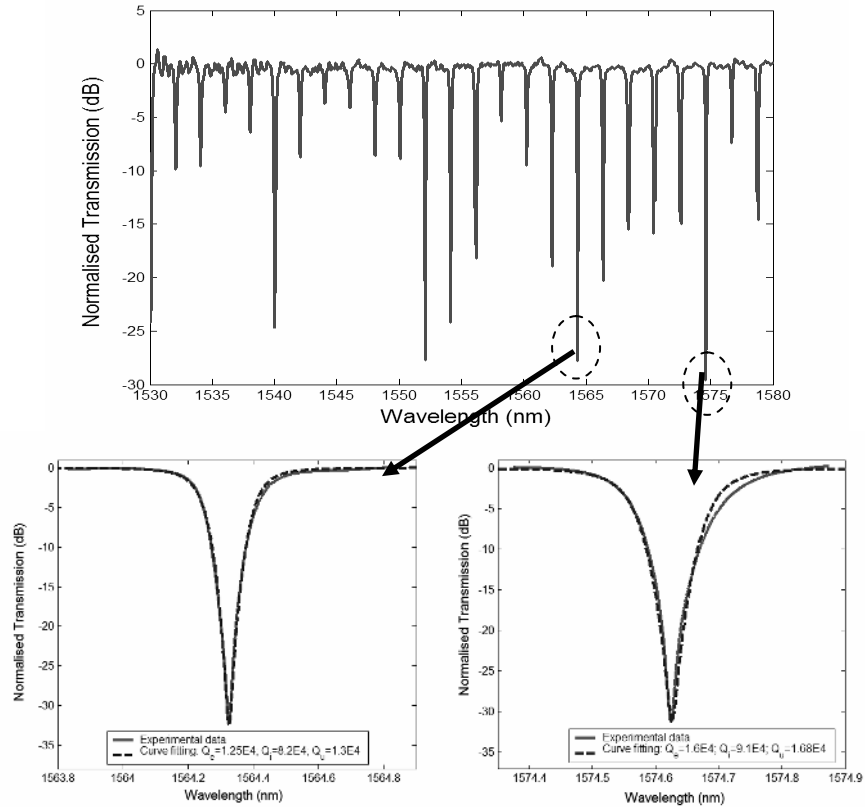
Fig. 5-11 Measured transmission spectra verses fitted curves for the microring resonator with the same geometry on single crystalline SOI.

5.3 Summary and thesis novelty

The thesis has presented a general cycle in silicon-based photonic device research, design, fabrication and characterisation.

The design work is carried out using various packages of simulation tools. For small-scale individual device such as the design of waveguides and micro-cavities, serial FDTD simulation seems sufficient. Where a few components are coupled, parallel simulation is inevitable for relatively fast design. However, one should not rely entirely on numerical simulations. Conventional method such as coupled-mode analysis and beam propagation methods are often adopted in the first place for the functionality design and validation. 2D simulations can be used to validate the functionality design in a coarse way and help determine the key parameters in the system. Rigorous but time-consuming 3D simulations can then be used to verify the design and fine-tune the structure. In this thesis, some high-Q cavities and resonant channel drop filters have been designed in 2D photonic crystal platform. A variety of light injecting methods have been studied in an attempt to improve the coupling between SMF and SOI waveguides.

The fabrication process involves interleaving steps of material deposition, lithography, etching and metallization. Compared to commercial SOI wafers fabricated using expensive wafer-bonding technology, PECVD provides full control of the vertical

structure. Flexible thickness and multi-layer structures can be achieved. E-beam lithography is used extensively to generate nanometer-scaled patterns. Depending on the design structure, both positive resist (ZEP 520A) and negative resist (maN 2405) are used. The issue of proximity effect is addressed manually according to the structure geometry. The stitch error is minimized by choosing proper write-field sizes and careful write-field alignment. The etching is done in ICP using fluorocarbon chemistry. Single-resist-layer lift-off process generates metal wires with width down to 200 nm.

The characterisation technique has been changed from high-loss and time-consuming butt-coupling method to efficient and simple vertical fiber-grating coupling method. The fiber-to-fiber loss has decreased from ~ 50 dB to ~ 20 dB. The sample needs no cleaving and the device can be fully contained in one E-beam write field.

To my best knowledge, the thesis has presented significant novelty in the following areas.
1. Ultra-compact channel add-drop filter in 2D PCS using a single degenerate cavity system has been designed for the first time (See paper III), indicating the possible implementation of photonic crystal for compact filters in future photonics.
2. Surface-mode filter in 2D amorphous silicon PhC has been experimentally demonstrated for the first time (See paper VII). This promotes our idea of "using PhC only where necessary". PhC may not become the leading platform for the next generation photonics but likely PhC micro-cavities will be integrated in photonic circuits locally where necessary.
3. High Q (5.6×10^{4}) and low-loss (15.30 dB/cm) amorphous silicon micro-silicon ring resonators have been demonstrated for the first time (See paper XI). The results have shown the possibility of using amorphous silicon in high-quality photonic devices.
4. The mutual mode coupling within a single ring and the inter-ring mode coupling between concentric rings have been thoroughly studied and experimentally demonstrated on SOI platform for the first time (See paper XII). Mutual mode coupling offers another freedom when designing ring-resonator-based filters. Concentric-ring results might be significant in bio-sensing applications as the inter-ring mode coupling increases the modal area and the transmission notch depth simultaneously.

5.4 Future prospects

There are some issues that have not been well-addressed during my three-year PhD and I would like to see follow-up work on them.

1. The dynamic response of the micro-ring resonators with mutual coupling for inputs of different signal formats. Eq. (6) gives the frequency response of the micro-ring filter. Due to mutual coupling, the line-shape in general is not Lorentzian. It would be interesting to see how the output signal is affected for different inputs, such as a square pulse, a Gaussian pulse or other modulated formats, and what happens when the combination of Q_e, Q_i and Q_u changes.

2. Multiple concentric rings for bio-sensing applications. I have shown that the double-ring filter offers much enhanced notch depth and larger mode area than the single-ring filter. The work is done at the very end of my PhD. I would like to further the research on multiple concentric rings and their applications in bio-sensing.

3. Experiments of the inverse taper mode converters. From Section 2, this converter offers higher coupling efficiency than gold gratings. It does not require a large vertical space and is good for integration. I have developed techniques to make the inverse taper waveguide with tip size below 100 nm. However, due to the difficulty in linking the E-beam process with photolithography and limited amount of time, I have not done any experiments on this type of converter. Though gold grating couplers provide many advantages, inverse taper mode converters are well-suited for commercial device as it offers easier solution for packaging. More research work on inverse taper converter is highly demanded.

4. Experiments of the membrane-type photonic crystal cavities and add-drop filters. I have done much simulation work on high Q photonic crystal cavities and add-drop filters. However, many designs are left without being experimentally demonstrated, especially for membrane-type photonic crystal devices.

References:

1. J. D. Joannopoulos, R. D. Meade, and J. Winn, Photonic Crystals: Modeling the Flow of Light, 1st ed. (Princeton University Press, Princeton, NJ,1995).

2. F. Ramos-Mendieta and P. Halevi, "Surface electromagnetic waves in two-dimensional photonic crystals: Effect of the position of the surface plane," Phys. Rev. B **59**, 15 112 (1999).

3. J. K. Yang, S. H. Kim, G. H. Kim, H. G. Park, Y. H. Lee, and S. B. Kim, "Slab-edge modes in two-dimensional photonic crystals," Appl. Phys. Lett. **84**, 3016 (2004).

4. S. Xiao and M. Qiu, "Surface mode microcavity," Appl. Phys. Lett., **87**, 111102 (2005).

5. T. J. Kippenberg, S. M. Spillane, D. K. Armani, and K. J. Vahala, "High-Q ring resonators in thin silicon-on-insulator," Appl. Phys. Lett. **83**, 797 (2003).

6. J. Niehusmann, A. Vörckel, P. H. Bolivar, T. Wahlbrink, W. Henschel, and H. Kurz, "Ultrahigh-quality-factor silicon-on-insulator microring resonator," Opt. Lett. **29**, 2861 (2004).

7. S. Xiao, M. H. Khan, H. Shen, and M. Qi, "Compact silicon microring resonators with ultra-low propagation loss in the C band," Opt. Express **15**, 14467 (2007).

8. P. Dumon, W. Bogaerts, V. Wiaux, J. Wouters, S. Beckx, J. V. Campenhout, D. Taillaert, B. Luyssaert, P. Bienstman, D. V. Thourhout, and R. Baets, "Low-Loss SOI Photonic Wires and Ring Resonators Fabricated With Deep UV Lithography," IEEE Photon. Tech. Lett, **16**, 1328 (2004).

9. B. E. Little, S. T. Chu, H. A. Haus, J. Foresi, and J. P. Laine, "Microring resonator channel dropping filters," IEEE J. Light. Tech. **15**, 998 (1997).

10. C. Manolatou, M. J. Khan, Shanhui Fan, Pierre R. Villeneuve, H. A. Haus, and J. D. Joannopoulos, "Coupling of Modes Analysis of Resonant Channel Add-Drop Filters," IEEE J. Quantum Electron. **35**, 1322 (1999).

Chapter 6. Guide to selected papers and account of original work

Paper I

Small-volume Waveguide-section High Q Microcavities in 2D Photonic Crystal Slabs

Z. Zhang and M. Qiu

Optics Express **12**, 3988-3995 (2004)

A series of microcavities in 2D hexagonal lattice photonic crystal slabs are studied in this paper. The microcavities are small sections of a photonic crystal waveguides. Finite difference time domain simulations show that these cavities preserve high Q modes with similar geometrical parameters and field profile. Effective modal volume is reduced gradually in this series of microcavity modes while maintaining high quality factor. Vertical Q value larger than 10^6 is obtained for one of these cavity modes with effective mode volume around 6.0 cubic half wavelengths $[(\lambda/2n_{slab})^3]$. Another cavity mode provides even smaller mode volume around 2.25 cubic half wavelengths, with vertical Q value exceeding 10^5.

Contributed by the author: I designed the cavities by 3D simulations and analysed the cavities in the momentum space.

Paper II

Influence of structural variations on high-Q microcavities in two-dimensional photonic crystal slabs

Z. Zhang and M. Qiu

Optics Letters **30**, 1713-15 (2005)

The influence of some critical structural variations is investigated on high Q microcavities in 2D photonic crystal slabs. All the cavities studied remain high Q in a wide range of structural variations, while the resonant frequencies shift in a relatively large scale when the structural variations are comparable to the physical sizes of the cavities.

Contributed by the author: I carried out the numerical analysis by 3D simulations.

Paper III

A compact design of in-plane channel drop filter using a single cavity with two degenerate modes in 2D photonic crystal slabs

Z. Zhang and M. Qiu

Optics Express **13**, 2596-2604 (2005)

A compact design of in-plane channel drop filter in 2D hexagonal lattice photonic crystal slabs is presented in this paper. The system consists of two photonic crystal waveguides and a single cavity with two degenerate modes. Both modes are able to confine light strongly in the vertical dimension and prove to couple equally into the waveguides. Three dimensional finite difference time domain simulations show that the quality factor is around 3,000. At resonance, power transferred to the drop waveguide is 78% and only 1.6% remains in the bus waveguide. We also show that by carefully tuning the drop waveguide boundary, light remaining in the bus can be further reduced to below 0.4% and the extinction ratio is larger than 22dB.

Contributed by the author: I designed the filter and analysed its performance.

Paper IV

Coupled mode analysis of in-plane channel drop filter with resonant mirrors

Z. Zhang and M. Qiu

Photonics and Nanostructures - Fundamentals and Applications **3**, 84-89 (2005)

The operation of resonant channel drop filters is analyzed using coupled mode theory in time. The resonator is chosen to support a single standing wave mode and 100% in-plane channel transfer can be realized by properly applying mirror boundary conditions to the waveguides. The analysis is verified by two dimensional finite difference time domain (2D FDTD) simulations in 2D hexagonal photonic crystals.

Contributed by the author: I designed the filter and analysed its performance.

Paper V

Coupled mode analysis of resonant channel drop filter using waveguides with mirror boundaries

Z. Zhang and M. Qiu

Journal of the Optical Society of America B (Optical Physics) **23**, 104-13 (2006)

The operation of in-plane channel drop filters with mirror boundaries is analyzed using coupled mode theory. The mirror is realized by a single mode cavity placed above or below a waveguide. The conditions to achieve 100% in-plane channel transfer are derived. The analysis is verified by two dimensional finite difference time domain simulations in 2D hexagonal photonic crystals.

Contributed by the author: I designed the filter and analysed its performance.

Paper VI

Parallel Power Computation for Photonic Crystal Devices

U. Andersson, M. Qiu, and Z. Zhang

Methods and Applications of Analysis, vol. **13**, 149-156 (2006)

Three-dimensional finite-different time-domain (3D FDTD) simulation of photonic crystal devices often demands large amount of computational resources. In many cases it is unlikely to carry out the task on a serial computer. We have recently parallelized an FDTD code with one-dimensional topology so that the computation domain can be divided into slices perpendicular to the direction of power flow. Though the speed-up of the parallelized code still leaves much for improvement, we are able to solve large-scale and long-running problems. Two cases are studied, i.e., the power transmission in a two-dimensional photonic crystal waveguide in a multilayered structure and the power coupling from a wire waveguide to a photonic crystal slab. In the first case, a power dip due to TE/TM modes conversion is observed and in the second case, the structure is optimized to improve the coupling.

Contributed by the author: I participated in the parallelization process for power computations with one-dimensional topology in the 3D FDTD code.

Paper VII

Optical filter based on two-dimensional photonic crystal surface-mode cavity in amorphous silicon-on-silica structure

Z. Zhang, M. Dainese, L. Wosinski, S. Xiao, M. Swillo, U. Andersson, and M. Qiu

Applied Physics Letters **90**, 041108 (2007)

An optical filter based on side coupling between silicon wire waveguide and two-dimensional photonic crystal surface-mode cavity is presented. The design is first

optimized numerically by parallel three-dimensional finite-different time-domain simulations. The device is then fabricated on amorphous silicon-on-silica structure. The drop wavelength is observed around 1580nm. The extinction ratio of the filter is larger than 10 dB and the intrinsic quality factor of the surface-mode cavity is approximately 2,000.

Contributed by the author: I designed, fabricated and characterized the optical filter proposed.

Paper VIII

Subwavelength-diameter Silica Wire for Light In-coupling to Silicon-based Waveguide

Z. Zhang, M. Qiu, U. Andersson, and L. Tong

Chinese Optics Letters **5**, 577 (2007)

Coupling between subwavelength-diameter silica wires and silicon-based waveguides is studied using the parallel three-dimensional (3D) finite-different time-domain method. Conventional butt-coupling to a silica-substrated silicon wire waveguide gives above 40% transmission at the wavelength range from 1300 to 1750 nm with good robustness against axial misalignments. Slow light can be generated by counter-directional coupling between a silica wire and a two-dimensional (2D) silicon photonic crystal slab waveguide. Through dispersion-band engineering, 82% transmission is achieved over a coupling distance of 50 lattice constants. The group velocity is estimated as 1/35 of the light speed in vacuum.

Contributed by the author: I simulated and analysed different light-injecting methods from silica fiber to silicon-based waveguide.

Paper IX

Subwavelength-diameter Silica Wire and Photonic Crystal Waveguide Slow Light Coupling

Z. Zhang, U. Andersson, and M. Qiu

Active and Passive Electronic Components, special issue on Metamaterials, Plasmonics, and THz Frequency Photonic Components , Volume 2007, Article ID 78602 (2007)

Counter-directional coupling between subwavelength-diameter silica wire and single-line-defect two-dimensional photonic crystal slab waveguide is studied

numerically using parallel three-dimensional finite-different time-domain method. By modifying silica wire properties or engineering photonic crystal waveguide dispersion band, the coupling central wavelength can be moved to the slow light region and the coupling efficiency improves simultaneously. One design gives 82% peak power transmission from silica wire to photonic crystal waveguide over an interacting distance of 50 lattice constants. The group velocity is estimated as 1/35 of light speed in vacuum.

Contributed by the author: I simulated and analyzed slow-light coupling mechanism between silica wire and photonic crystal waveguide.

Paper X

Optically Tunable Delay Line in Silicon Microring Resonator Based on Thermal Nonlinear Effect

F. Liu, Q. Li, <u>Z. Zhang</u>, M. Qiu, and Y. Su

To be published in IEEE. Journal of Selected Topics in Quantum Electronics (2008)

We experimentally demonstrate optically tunable delay line in a silicon microring resonator with a 20-μm radius. The delay-tuning mechanism is based on the red shift of the resonance induced by thermal nonlinear effect. We investigate the delay performance of three modulation formats: non-return-to-zero (NRZ), return-to-zero (RZ) and differential phase shift keying (DPSK) signals at different data rates. Tunable delay is achieved by controlling the power of the continuous wave (CW) pump with very low tuning threshold, which could be used in microring resonator based slow-light structure.

Contributed by the author: I fabricated the ring resonators.

Paper XI

High-quality-factor micro-ring resonator in amorphous-silicon on insulator structure

<u>Z. Zhang</u>, M. Dainese, M. Chacinski, L. Wosinski, and M. Qiu

Submitted for journal publication (2008)

A 40-μm-radius micro-ring resonator is fabricated in hydrogenated amorphous silicon (α-Si:H) on silica structure. Curve fitting by coupled mode theory shows that the intrinsic quality factor is 56,000 for the resonant mode at 1539.2 nm and the notch depth is around 30 dB. The intrinsic loss per unit length in the ring is 15.3 dB/cm, comparable to 9.16 dB/cm in the single-crystalline silicon ring of the same geometry. The results indicate the possible implementation of amorphous silicon for high quality optical filters.

Contributed by the author: I fabricated the ring resonators, characterized the devices and analyzed the data.

Paper XII

Resonance-splitting and enhanced notch depth in SOI ring resonators with mutual mode coupling

Z. Zhang, M. Dainese, L. Wosinski, and M. Qiu

Resonance-splitting and enhanced notch depth are experimentally demonstrated in micro-ring resonators on a SOI platform as a result of the mutual mode coupling. This coupling can be generated either by the nanometer-scaled gratings along the ring sidewalls or by evanescent directional coupling between two concentric rings. The transmission spectra are fitted using the time-domain coupled mode analysis. Split-wavelength separation of 0.68 nm for the 5-μm-radius ring, notch depth of 40 dB for the 10-μm-radius ring, and intrinsic Q factor of 2.6×10^5 for the 20-μm-radius ring are demonstrated. Notch depth improvement larger than 25dB has been reached in the 40-39-μm-radius double-ring structure. The enhanced notch depth and increased modal area for the concentric rings might be promising advantages for bio-sensing applications.

Contributed by the author: I fabricated the ring resonators, characterized the devices and analyzed the data.